Engineering optical lattices in k-space

ETH
Eidgenössische Technische Hochschule Zürich
Swiss Federal Institute of Technology Zurich

D PHYS

Samuel Jele

Engineering optical lattices in k-space

Master Thesis

Department of Physics
Swiss Federal Institute of Technology (ETH) Zurich

Supervision

Marius Gächter
Dr. Konrad Viebahn
Prof. Tilman Esslinger

April 2023

Contents

Abstract

In this thesis we report on the further development of the superlattice accordion, conceived during the master thesis of S. Wili (S. Wili *et al.*, 2023). They propose two superimposed accordion lattices as a tool for increasing inter-atomic distance in an optical lattice to arbitrary values. The accordion lattices will be controlled using acousto-optical deflectors (AODs), which require long beam paths in combination with an active lattice phase stabilization. In the first part of this thesis we generalize the theory of the active feedback scheme to two-dimensional lattices. The approach is theoretically validated by a simulation of the phase measurement procedure involved. We then propose an implementation of the digital AOD driving tone synthesis. For this we compared various options for digitally generating the required radio-frequency (RF) tones and chose the Software Defined Radio USRP N310 by Ettus Research (NI). The second part of the thesis is concerned with the design and implementation of a high-power 532 nm laser source for the lattice beams, using second harmonic generation (SHG). The required output power for this laser source is 12 W using a maximum of 45 W of 1064 nm input power. We use a MgO doped sPPLT with a poling period of 7.98 µm as the nonlinear crystal to double the 1064 nm, 45 W laser source from Azurelight Systems (ALS). A Peltier element is used for establishing the phase matching temperature of the nonlinear crystal. At an input power of 34.75 W we achieve an output power of 14.1 W, which equates to a conversion efficiency of 40.6 %. The monolithic setup designed during this thesis, which is machined from a single piece of aluminum to minimize dust pollution and increase temperature stability, offers a compact and reproducible setup for SHG. With this monolithic setup we achieve a temperature stability of 0.002 °C. We encountered drops in the conversion efficiency during a long-term measurement, which can be attributed to mode jumps of the seed laser of the ALS, but further investigation is necessary.

Chapter 1

Introduction

The field of analog quantum simulation with ultra-cold atoms has attracted an increasing amount of research in the recent years. It has evolved into a serious competitor to universal quantum computers in terms of practical use [1]. The latter, based on, for example, superconducting qubits [2], spin qubits in Quantum Dots [3] or nitrogen vacancies [4], aims to provide a quantum enhanced version of the classical computer, on which physicists have implemented simulations of real systems for decades. Analog quantum simulations take a different route. The key idea is to build a well-controllable model that describes or approximates the behaviour of a real-world system, the most prominent example being the Hubbard model [5]. Systems in which interactions play a major role are especially interesting, since their simulation on classical computers is very challenging or even impossible. The Lattice Team in the Quantum Optics group of Prof. Tilman Esslinger at ETH Zurich implements such an analog quantum simulator with ultra-cold atoms in an optical lattice. Special research interest is directed to the interplay of topology and interactions [6, 7, 8]. In general, the hope is that analog quantum simulation can help answer some of the most interesting open questions, especially in condensed matter physics. The most prominent example probably being the possibility of d-wave pairing in the Hubbard model [9].

Condensed matter physics is primarily concerned with the behaviour of electrons in periodic crystal structures. This system can be simulated with ultra-cold atoms in optical lattices. The atoms take over the role of the electrons, and the crystal potential is realized using the attractive force to maxima or minima of the intensity in optical the lattice [10]. Bloch theory shows that non-interacting electrons in a periodic potential are described by Bloch waves, which are essentially plane waves modulated by functions that share the symmetry of the crystal [11]. It is possible to approximate this description with a lattice model using Wannier states [12], where localized electrons are described on lattice sites with finite tunneling probability to nearest- or next-nearest neighbours. The tunneling rates are determined by the overlap of localized states [12]. The simplest form of interaction that can be added to a lattice model is an on-site interaction (this is essentially the Hubbard model), where atoms only feel the presence of each other when they reside on the same lattice site. Ultra-cold atoms in optical lattices offer excellent control over these two defining model parameters: the on-site interaction strength can be tuned using Feshbach resonances and the tunneling rate is controlled by the lattice depth [10].

Just as important as controlling model parameters is the ability to observe the behaviour of the system. Here, the current setup of the Lattice Team only gives access to averages and thermodynamic quantities, such as average number of double-occupied sites or averaged spin correlations. But for the investigation of strongly-interacting systems, topological phases of matter and strongly-correlated phases of matter, access to microscopic observables such as site-resolved spin correlations

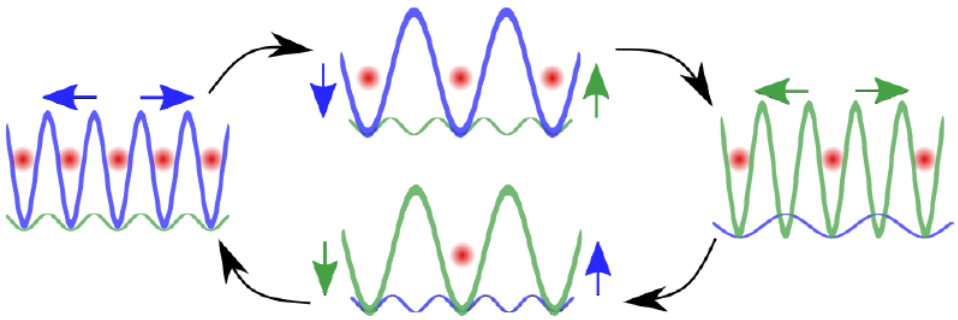

Figure 1.1: One cycle of the accordion superlattice expansion. Here explained on the example of an initially half-filled lattice (one atom per lattice site). The blue lattice (lattice A) is expanded by a factor of two. Then, an additional lattice (lattice B, green) with the original lattice constant is ramped up and lattice B is ramped down. This leaves an atom in every second lattice site of lattice B. Then lattice B is expanded by a factor of two. This procedure can be repeated to reach, in principal, arbitrary atom separation. Figure taken from Ref. [13].

or single-site resolved atom detection offers great insight into such states [12]. In order to close this gap, the Lattice setup will be updated to offer, besides other new features, single site resolution using a novel technique involving an accordion superlattice developed in Ref. [13].

An accordion lattice refers to an optical lattice with variable lattice constant [13]. The key idea of the superlattice accordion is to increase the inter-atomic distance by periodically loading atoms into resized optical lattices. Figure 1.1 shows one cycle of such an expansion. After the experimental run, the lattice (lattice A) is ramped up to freeze the atoms on site. Then, the lattice constant is doubled using acousto optical deflectors (AODs). After this expansion, an additional lattice (lattice B) with the original lattice constant is ramped up while lattice A is ramped down. This procedure can then be repeated to reach, in principle, arbitrary atom separation. In order to achieve the dynamic range necessary for doubling the lattice constant, long beam paths cannot be avoided [13]. This increases phase fluctuations of the lattice beams due to temperature- and pressure variations which impacts the lattice stability, as we will show in the next chapter. In order to prevent phase mismatch during the hand-over process, an active phase stabilization will be implemented. This will also be helpful for the alignment of the two superimposed accordion lattices during the expansion process.

In this thesis we will further develop the feedback scheme for the lattice phase stabilization. In chapter two, we will extend the theory of phase measurement using an image of the lattice and Fourier transform from Ref. [14] to a two dimensional lattice. With a simulation of this measurement method will determine the necessary performance of the camera used for the lattice imaging. Also choosing an appropriate frequency source for the AODs, which will be at the heart of this feedback scheme, will be discussed. In chapter three, we present the development of a 532 nm laser source for the optical lattice using second harmonic generation (SHG) [15]. For this purpose, a power of 12 W is required. We start by giving an overview of the theory of SHG and (quasi) phase matching. Then we show the calculations for the correct experimental parameters for reaching high conversion efficiency. We also design a monolithic setup and present efficiency, beam shape and stability measurements performed on this setup. Chapter four will summarize the results and give an outlook on further developments of this part of the new Lattice setup.

Chapter 2

Lattice stabilization

2.1 Optical lattices

The accordion lattice expansion technique utilizes two superimposed two-dimensional (2D) optical lattices, where the second lattice has twice the lattice constant of the first. Each lattice is generated by letting four laser beams interfere with each other; two per x- and y-direction (we describe the lattice in the xy-plane). Let us first consider one lattice consisting of four incident beams. We will approximate the laser beams in this section as plane waves, which is sufficient for this treatment (more details can be found in Ref. [13]). Hence we write

$$E_{\alpha,i}(\alpha, z, t) = \sqrt{I^{(0)}_{\alpha,i}} \cos\left(\pm k\alpha + k_{\parallel} z - \omega t + \phi_{\alpha,i}\right), \tag{2.1}$$

where $\alpha = x, y$ and where we use the index $i = 1$ for waves traveling in positive and $i = 2$ in negative α direction. We have also assumed that the wavevectors either have a non-zero x- or a non-zero y component; in other words, the wavevectors of the beam along the x and y direction are orthogonal. The total field is then given by

$$E(x, y, t) = \sum_{\substack{\alpha=x,y \\ i=1,2}} E_{\alpha,i}(\alpha, t). \tag{2.2}$$

The intensity can be split into three parts:

$$I(x, y) = \langle E^2(x, y, t)\rangle_t = I_x(x) + I_y(y) + I_{xy}(x, y), \tag{2.3}$$

where $\langle f(t)\rangle_t$ is the time average of the function $f(t)$ (the time average is taken over many optical oscillations). The first two terms arise from the interference of beams along the same axis, and the third term is the cross-interference between beams along the x- and the y-axis. We use the identity $\cos(a) + \cos(b) = 2\cos(\frac{a+b}{2})\cos(\frac{a-b}{2})$ and the definitions $\Delta\phi_\alpha = \phi_{\alpha,1} - \phi_{\alpha,2}$ and $\Sigma_\alpha = \phi_{\alpha,1} + \phi_{\alpha,2}$ to write

$$I_\alpha(\alpha) = 2I^{(0)}_\alpha \cos^2\left(k\alpha + \frac{\Delta\phi_\alpha}{2}\right) \tag{2.4}$$

$$I_{xy}(x, y) = \sqrt{I^{(0)}_x I^{(0)}_y} \cos\left(kx + \frac{\Delta\phi_x}{2}\right) \cos\left(ky + \frac{\Delta\phi_y}{2}\right) \cos\left(\frac{\Sigma_x - \Sigma_y}{2}\right). \tag{2.5}$$

Here we have used $\langle\cos^2(k\alpha + \Delta\phi_\alpha/2)\rangle_t = 1/2$ and $\langle\cos(\omega t - \Sigma_y/2)\cos(\omega t - \Sigma_y/2)\rangle_t = \frac{1}{2}\cos(\Sigma_x/2 - \Sigma_y/2)$. We also assumed equal intensities of the two counterpropagating beam pairs.

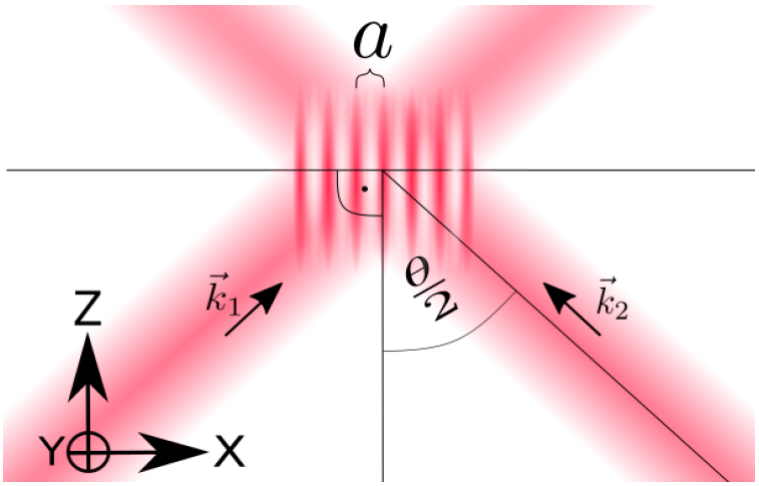

Figure 2.1: Example of a one dimensional lattice formed by two interfering laser beams. The lattice constant a is determined by the wavelength λ and the angle θ between the two laser beams. When the beams travel anti-parallel ($\theta = 180°$), then the smallest possible lattice is formed with $a = \lambda/2$. Figure taken from Ref. [13].

We see that the lattice constant a_α of the arising optical lattice in α-direction is determined by the projection k_α of the total wavevector $(k, 0, k_\parallel)^T$ or $(0, k, k_\parallel)^T$ onto the xy-plane. It is given by

$$a_\alpha = \frac{\lambda}{2 \sin \theta_\alpha / 2}, \tag{2.6}$$

where λ is the wavelength of the laser beams and $\theta_\alpha = 2 \arctan k/k_\parallel$ is the angle of the counterpropagating beams in α-direction, as depicted in Figure 2.1 for $\alpha = x$. Therefore, we can control the lattice constant by tuning the angle θ. The smallest possible lattice constant is given by $a_{\min} = \lambda/2$.

The relative phases $\Delta\phi_x$ and $\Delta\phi_y$ control the position of the lattice, whereas the sum term $\Sigma_x - \Sigma_y$, also called the superlattice phase, determines the lattice geometry. In Figure 2.2(a)-(b) we show examples of intensity patterns with different superlattice phases. We will define

$$\varphi = \Sigma_x - \Sigma_y. \tag{2.7}$$

Notice that, for certain combinations of phases, the cross-interference term vanishes when $\varphi = (2n + 1)\pi,\ n \in \mathbb{Z}$.

It is also worth thinking about the domains of phases that have to be considered, in order to construct every possible lattice. It is clear that the superlattice phase can be restricted to $\varphi \in [0, 2\pi)$, since then $\cos \varphi/2$ covers the full range $[-1, 1]$. Initially it may seem like we have to specify $\Delta\phi_\alpha$ in the interval $[0, 4\pi)$, since, e.g., $\Delta\phi_x = \pi$ and $\Delta\phi_x = 3\pi$ lead to different lattices (due to the $\cos(kx + \Delta\phi_x/2)$ term in the cross-intereference part of the intensity pattern). But the difference comes only down to the sign of the cross-interference term, since $\cos(k\alpha + \Delta\phi_\alpha/2) = -\cos(k\alpha + (\Delta\phi_\alpha + 2\pi)/2)$. We can collect all sign factors of $\cos(kx + \Delta\phi_x/2)$, $\cos(ky + \Delta\phi_y/2)$ and $\cos(\varphi/2)$, assign their product to the cosine part of the superlattice phase, and finally restrict $\Delta\phi_\alpha$ to $[0, 2\pi)$, in order to get uniquely defined phases.

We see from equations 2.4 and 2.5 that $\Delta\phi_x$, $\Delta\phi_y$ and φ fully determine the position and geometry of the lattice. This leaves one of the four beam phases as a physical irrelevant parameter and hence it can be fixed to an arbitrary value. We choose to set

$$\phi_{y,2} = 0. \tag{2.8}$$

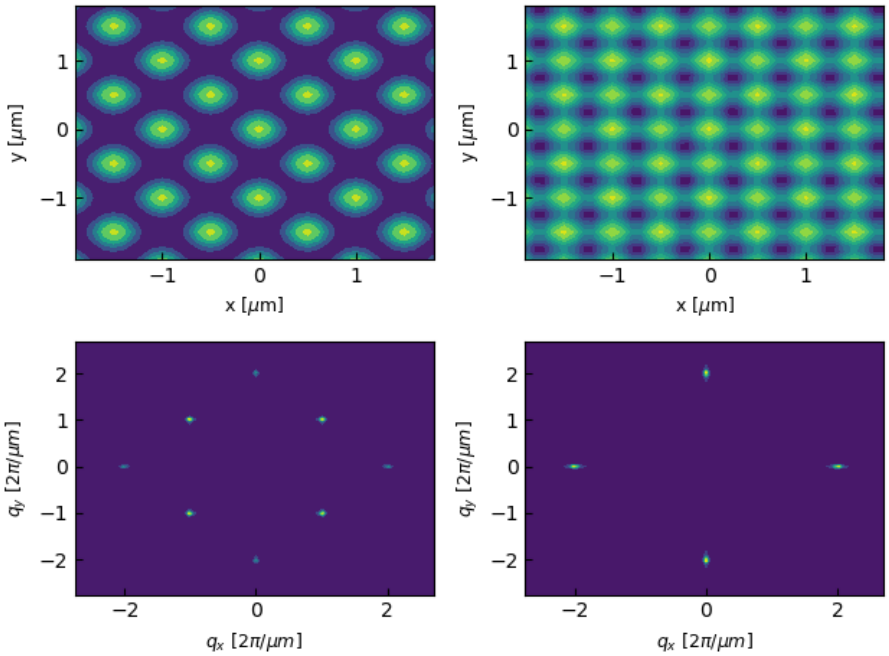

Figure 2.2: Top row: Two examples of two dimensional optical lattices (from simulation, $\lambda = 0.5\,\mu\text{m}$, $k = 0.5\frac{2\pi}{\lambda}$) with different superlattice phase $\varphi = 0$ (left) and $\varphi = \pi$ (right). Bottom row: Fourier transform of the respective lattice. In the intensity pattern with $\varphi = 0$ the cross-interference term containing $\cos\varphi/2$ has full contrast. This can be seen in the Fourier transform of the pattern in the bottom left. The delta peaks at (k, k), $(k, -k)$, $(-k, k)$ and $(-k, -k)$ are clearly visible. In contrast, the pattern with $\varphi = \pi$ has no cross-interference part, since $\cos\varphi/2 = 0$. The Fourier transform only shows the delta peaks at $(\pm 2k, 0)$ and $(0, \pm 2k)$ from the interference of the counterpropagating beams. Note that the delta peak at $(0, 0)$ has been suppressed in order to enhance contrast.

From this treatment we can see that when we have two sets of four laser beams, one with wavevectors k, frequency ω and the other with wavevectors $k/2$ and frequency 2ω, we can write the arising intensity pattern as the sum of two independent set of optical lattices, because any cross-interference of laser beams with different frequencies is averaged to zero.

2.2 Phase measurement

The choice of AODs to control the lattice angles necessarily leads to long beam paths in the experiment. Therefore, larger lattice phase fluctuations can be anticipated. On the one hand, vibrations can lead to fluctuations on the kHz scale, which we plan to mitigate by a monolithic optics design. On the other hand, there will be unavoidable slow drifts (on the Hz timescale) due to changes in ambient pressure, temperature and/or humidity. From above we see that this will impact the stability of the position and geometry of the lattice, through fluctuations in $\Delta\phi_\alpha$ and φ, respectively. Consequently, an active phase stabilization is required. In a feedback loop we have to be able to measure the current value of each of these phases. In the following we will show how this information can be extracted from the spatial Fourier transform of the image of the intensity pattern.

For the two dimensional Fourier transform we will use the convention

$$\mathcal{F}[f(x,y)](q_x,q_y) = \frac{1}{(2\pi)^2}\int dxdy\ f(x,y)e^{-iq_x x - iq_y y}, \tag{2.9}$$

and write $I(q_x,q_y) = I_x(q_x,q_y) + I_y(q_x,q_y) + I_{xy}(q_x,q_y)$ for the Fourier transform of the intensity. Using the well-known Fourier transform identity

$$\mathcal{F}[e^{ikx}] = \delta(q_x - k)\delta(q_y), \tag{2.10}$$

we find

$$I_\alpha(q_\alpha, q_{\bar{\alpha}}) = I_\alpha^{(0)}\left[\delta(q_\alpha - 2k) + \delta(q_\alpha + 2k)\right] e^{i\Delta\phi_\alpha}\delta(q_{\bar{\alpha}}) \tag{2.11}$$

and

$$\begin{aligned} I_{xy}(q_x,q_y) = \frac{\sqrt{I_x^{(0)} I_y^{(0)}}}{2}&\left[\delta(q_x - k) + \delta(q_x + k)\right] e^{i\Delta\phi_x/2}\times \\ &\left[\delta(q_y - k) + \delta(q_y + k)\right] e^{i\Delta\phi_y/2} \times \cos\left(\frac{\varphi}{2}\right). \end{aligned} \tag{2.12}$$

We have omitted the DC term proportional to $\delta(q_x)\delta(q_x)$, since it does not contain any phase information. We can then readily calculate the phases using

$$\Delta\phi_y = \arctan\left(\frac{\Im\{I(2k,0)\}}{\Re\{I(2k,0)\}}\right) \tag{2.13}$$

$$\Delta\phi_x = \arctan\left(\frac{\Im\{I(0,2k)\}}{\Re\{I(0,2k)\}}\right) \tag{2.14}$$

$$\varphi = 2\arccos\left(\frac{2e^{-i(\Delta\phi_x+\Delta\phi_y)/2}}{\sqrt{I_x^{(0)} I_y^{(0)}}} I(k,k)\right). \tag{2.15}$$

Recalling that we set $\phi_{y,2} = 0$, we find

$$\implies \phi_{y,1} = \Delta\phi_y \tag{2.16}$$

$$\implies \phi_{x,1} = \frac{1}{2}\left(\Delta\phi_x + \varphi + \phi_{y,1}\right) \tag{2.17}$$

$$\implies \phi_{x,2} = \frac{1}{2}\left(\phi_{x,1} - \Delta\phi_x\right) \tag{2.18}$$

There are a few things to note here. First, we see that the relative phases are calculated from the ratio of the imaginary and real part of the Fourier transform at the points $(2k,0)$ and $(0,2k)$. Hence the magnitude of the intensity cancels by default. This measurement is therefore not affected by fluctuations in the laser beam intensities and the relative phases can be extracted with excellent precision. This is not the case for the extraction of the superlattice phase. The intensity has to be normalized first before calculating the inverse cosine, as can be seen in equation 2.15. Thereby intensity fluctuations impact the precision of the superlattice phase measurement. Additionally, at superlattice phases close to π, the intensity at the point (k,k) in Fourier space vanishes. This can lead to problems in accuracy stemming from bad signal-to-noise ratio. In the following, a method to extract all required phases is described, which does not suffer from reduced precision due to the influence of intensity fluctuations and limited signal-to-noise ratio.

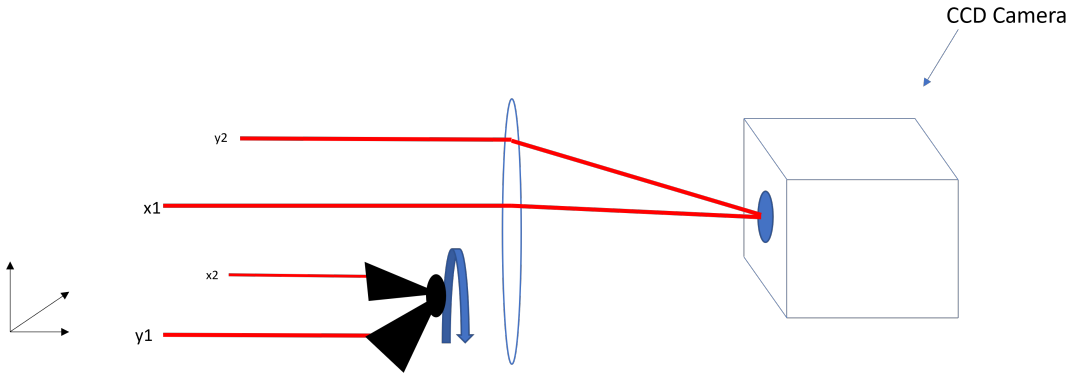

Figure 2.3: Schematic of the shutter method. This shows the situation after the glass cell, where the atoms sit, and a collimating lens. The shutter periodically blocks two of the four beams. From the resulting intensity pattern the relative phase between the non-blocked beams can be measured. Repeating this for two more pairs of blocked beams, all three relevant phases can be calculated. The shutter will rotate at constant speed. The FPGA has to be aware of the shutter position, in order to perform the correct phase extraction formula.

Shutter method

In general, the difference of phases of two counterpropagating beams can be extracted accurately. Therefore, the idea is to always measure pairs of beams instead of the full lattice potential. This can be achieved by blocking two of the four beams and measuring the phases pairwise. We will describe the procedure for the blocking of the beams traveling in negative x- and y direction. For different blocked pairs, the formulae have to be adjusted accordingly.

After blocking the beams traveling in negative x- and y-direction, the time-averaged intensity pattern is given by

$$\begin{aligned} I_{\text{shutter}}(x,y) &= \langle(\cos(kx+\phi_{x,1}-\omega t)+\cos(ky+\phi_{y,1}-\omega t)^2\rangle_t \\ &= 1+\cos\left(k(x-y)+\Delta\phi_{x1,y1}\right), \end{aligned} \tag{2.19}$$

where we defined $\Delta\phi_{x1,y1} = \phi_{x,1} - \phi_{y,1}$. The Fourier transform of this intensity pattern is then given by

$$I_{\text{shutter}}(q_x,q_y) = \delta(q_x-k)\delta(q_y+k)e^{i\Delta\phi_{x1,y1}} + \delta(q_x+k)\delta(q_y-k)e^{-i\Delta\phi_{x1,y1}}, \tag{2.20}$$

where we have again omitted the DC part and prefactors. From this we can calculate the relative phase as usual:

$$\Delta\phi_{x1,y1} = \arctan\left(\frac{\Im\{I_{\text{shutter}}(k,-k)\}}{\Re\{I_{\text{shutter}}(k,-k)\}}\right). \tag{2.21}$$

In the experiment, we will periodically block two of the four beams with a rotating shutter, as shown in Figure 2.3. This will allow us to calculate all relevant phases once per revolution.

In order to verify the concept of this phase extraction, we have implemented the method in a simulation, which is presented in the next section.

2.3 Simulation

With this simulation we will verify the phase extraction method developed above. In addition, we will derive minimal specifications for a camera that is used in the feedback scheme. The simulation

takes four (or eight for two superimposed lattices) wave vectors and phases as input parameters, calculates the corresponding (time-averaged) lattice and then again extracts the phases as described above. In the simulation we use plane waves with Gaussian envelope, i.e.

$$E_{\alpha,i}(x,y,z,t) = \exp\left(-\frac{(\mathbf{k}\times\mathbf{r})^2}{\mathbf{k}^2\sigma^2}\right)\cos\left(\pm k\alpha + k_\parallel z - \omega t + \phi_{\alpha,i}\right), \tag{2.22}$$

where $\mathbf{k} = (k, 0, k_\parallel)^T$ or $\mathbf{k} = (0, k, k_\parallel)^T$ and $\mathbf{r} = (x, y, z)^T$. The width of the Gaussian is given by σ. For all simulations shown here, $\sigma = 10\,\mu\text{m}$. With that choice, around 20x20 lattice sites are visible at $\theta = 120°$. Figure 2.2 (a) and (b) are example outputs of the intensity pattern calculated by the simulation. Figure (c) and (d) show the FFT calculated from these patterns. We see clear delta peaks at $(2k, 0)$, $(0, 2k)$ and $(\pm k, \pm k)$ when the superlattice phase is zero and the peaks at $(\pm k, \pm k)$ vanish when $\varphi = \pi$. We also want to show that treating the two superimposed lattices separately for the phase extraction is justified. The pattern and its Fourier transform can be seen in Figure 2.4. It is clear from that that the two lattices will not interfere with each others phase extraction.

To test the shutter method and the phase extraction in general, we randomly generate 50 pairs of phases, let the simulation calculate the according lattice for each pair of phases and compare the extracted phases to the input. In order to make the simulation more realistic, we have added random noise of amplitude 0.1 to the intensity pattern. In addition to that, we have quantized the image with 16 bit resolution to model a digital camera. The result can be seen in Figure 2.6. The extracted phases are marked with a tilde. We conclude that for all generated phase pairs, the extraction method works very well, with errors below 0.01 rad.

Now we will determine the minimal requirements for a camera, such as resolution and what field-of-view (FoV), to extract the lattice phases with a good precision. We have found that the resolution of the camera, i.e. pixel per lattice site, only has to fulfill Shannon's sampling theorem [16] (more than 2 pixel per lattice site). Higher resolution will not improve the phase extraction error. But on the other hand, the field of view is very important. We have found that for $\lambda = 0.5\,\mu\text{m}$ and $\theta = 120°$, a FoV of $10\,\mu\text{m}$ by $10\,\mu\text{m}$ is a lower limit. If the FoV is smaller than that, the phase extraction error quickly rises above 0.1 rad (tested with several different resolutions and for $\sigma = 10\,\mu\text{m}$ and $\sigma = 5\,\mu\text{m}$). This agrees with our expectations, since the resolution of the camera only gives the highest possible frequency we can detect, while the FoV gives the resolution in Fourier space. When the resolution in Fourier space is too small, we cannot access the value at the delta peaks accurately enough in order to extract the complex phase at this point. This we expect to be relatively independent of the size of the Gaussian beam, i.e. the number of lattice sites. When the beams become too small, the error again starts to rise. We found that below $\sigma = 3\,\mu\text{m}$, which gives approximately 6x6 visible lattice sites, the phase extraction error is above 0.1 rad.

With this simulation we have shown that the method for phase extraction, proposed in Ref. [14], also works for two-dimensional optical lattices. In the next section we will discuss the active part of the feedback loop, i.e. how we can control the phases of the lattice.

2.4 Active feedback

As explained in detail in the introduction, for the Lattice experiment we need to control the lattice constant, absolute position and the shape of both superimposed lattices. As we have seen in the previous section, these lattice parameters are determined by the angle θ and the laser beam phases. We can manipulate both by using acousto optical deflectors (AODs) [17]. Due to long beam paths that are unavoidable when using AODs, again referring to the introduction for a more detailed description, we also need an active phase stabilization.

The feedback scheme will be implemented using

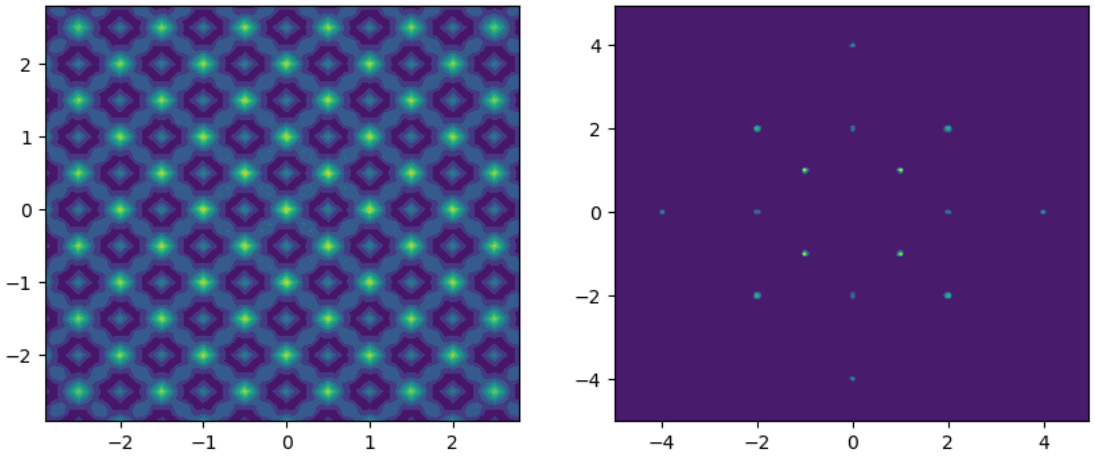

Figure 2.4: Left: Simulated intensity pattern of two superimposed lattices with the same wavelength $\lambda = 0.5\,\mu m$, the wavevectors $k = 0.5\frac{2\pi}{\lambda}$ and $k = \frac{2\pi}{\lambda}$ and all phases set to zero. Note that this is a zoomed-in image. The intensity pattern used to calculate the Fourier transform is $8\,\mu m$ by $8\,\mu m$. Right: Fourier transform of the double lattice. All delta peaks, especially from different lattices, are well separated.

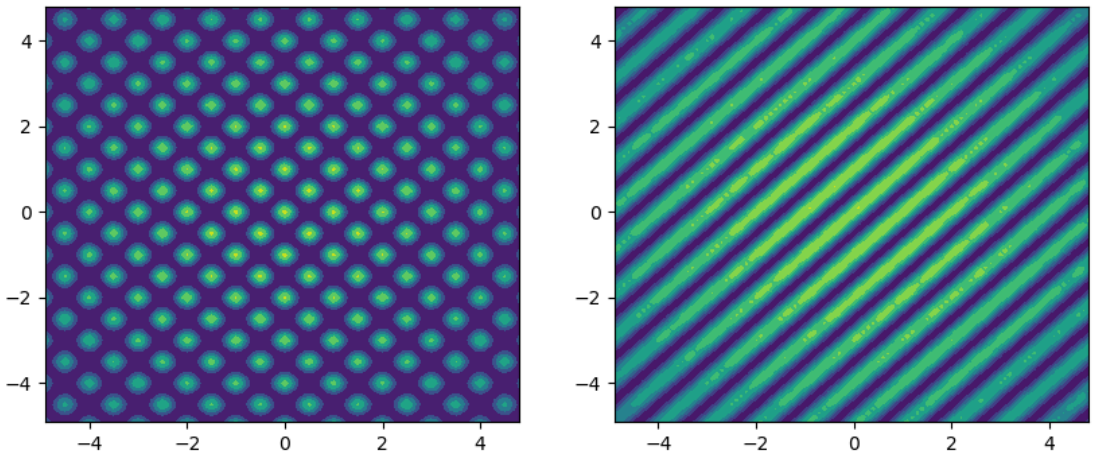

Figure 2.5: Left: Image of the full lattice, when all four beams reach the camera. Right: Intensity pattern when one of the x- and y-beams is blocked.

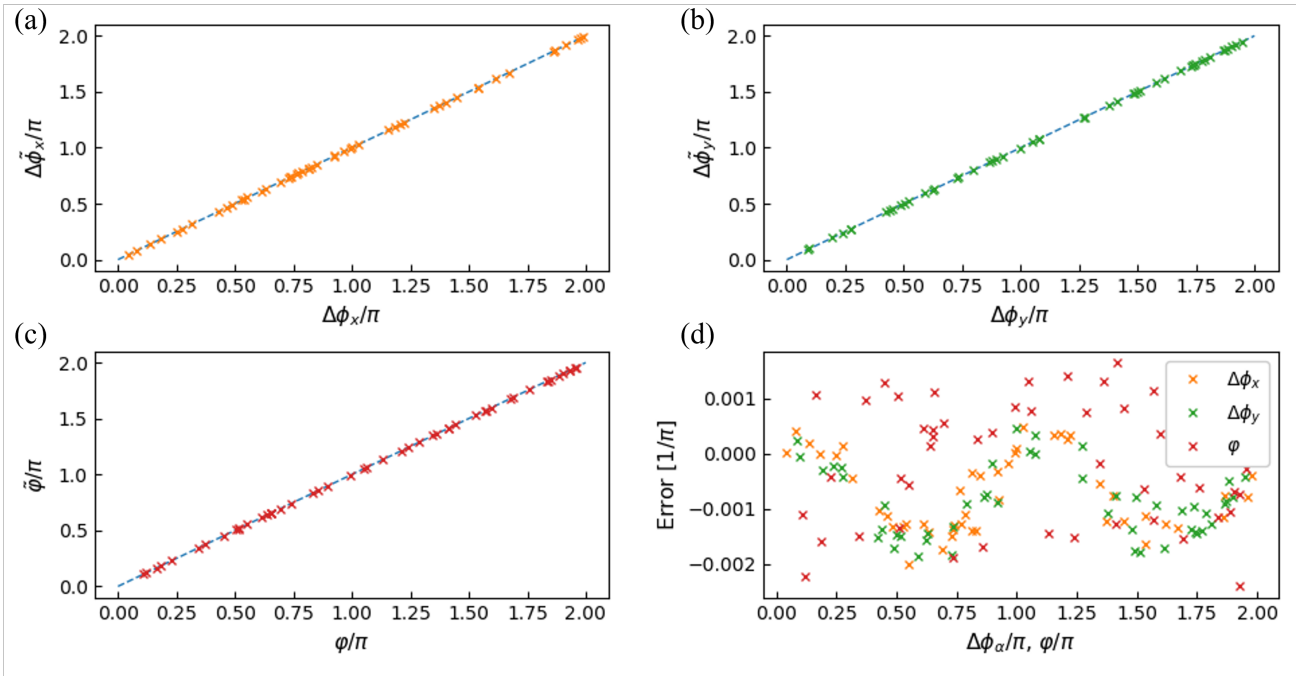

Figure 2.6: Phase extraction for 50 randomly generated phase pairs (simulation parameters: $\lambda = 0.5\,\mu\text{m}$, $\theta = 120°$, 2.9 pixel per lattice site and $32.8\,\mu\text{m}$ by $32.8\,\mu\text{m}$ field of view). The quantities on the x-axis denote the phase that was input into the simulation run, the quantities on the y-axis (with the tilde) denote the extracted phases. (a)-(c) show the the extracted phases as a function of the input phases. If the phase extraction works perfect, all points lie on the $y = x$ axis. (d) shows the absolute error. All errors are below 0.01 rad. There seems to be a clear functional dependence of the error of the relative phases $\Delta\phi_\alpha$ on the input relative phases. Also the error of the superlattice phases is equally distributed around zero error, while the relative phases are consistently underestimated by the phase extraction method.

.

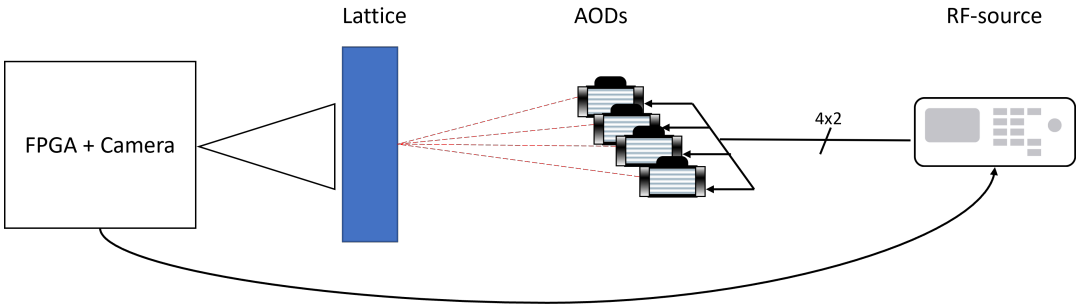

Figure 2.7: Block diagram of the feedback scheme. The camera images the lattice, the FPGA extracts the light phases and calculates the control signal for each AOD driving tone. This control signal is then sent to the RF-source that then acts back on the light phases. We estimate a necessary update rate of 1 ms for all phases.

- a CCD camera for imaging the lattice,
- an FPGA for calculating the FFT, extracting the phases and generating the phase control signals,
- four AODs for acting on the phases of the laser beams
- and a frequency source for driving the AODs, that can interpret the phase control signal and act on the AODs respectively.

It is shown in block diagram form in Figure 2.7. This places high demands on the frequency source for the AODs. Compiling all necessary features and, based on this compilation, justifying the choice of the frequency source will be the focus of this next subsection.

2.5 Digital RF (radio-frequency) sources for active lattice control

Active control over all lattice parameters, in particular the lattice spacing, the lattice phases, and the lattice depth, will be achieved using AODs. These are, in turn, driven by frequency sources in the radio frequency (RF) domain. In this section we will assess various digital frequency sources in order to choose the ideal device for our application.

In order to be able to choose the most optimal frequency source for the experimental setup, we first have to be aware of all the necessary features it has to offer. The AODs are not only part of the feedback loop, but are also used to control the lattice constant and intensity. This frequency source will therefore be used in the experimental sequence as well, e.g., for the accordion zoom-in. As can be seen in Figure 1.1, for this we need to be able to ramp the intensity of each lattice and also change then lattice constant continuously. The lattice constant can be controlled by changing the angle at which the laser beams interfere. This we can do by changing the driving frequency of the AODs, since it controls the deflection angle of the first order beam. The intensity of the lattice is simply the intensity of the laser beam that gets deflected by the AOD into the first order beam and is hence controlled by the intensity of the driving signal. Finally, the phases of the laser beams can be directly controlled by changing the phase of the driving signal. For the active lattice stabilization we want to be able to change all eight signal phases every 1 ms. For the experimental sequence as well as for the accordion zoom-in procedure, we have to be able to perform full scale amplitude- and frequency ramps on a time scale of 100 µs. The acceptance bandwidth of the AOD we will use in the setup is 75 MHz to 100 MHz [18]. We have also decided to only consider devices

that offer digital (most devices only offer analog-) modulation inputs (for amplitude, frequency and phase). This will simplify our setup, since we would otherwise need eight digital-to-analog converters for amplitude, frequency and phase modulation, each. Another very important detail is that for the frequency and phase modulation, the output signal must never have discontinuities[1]. This leads to the following list of necessary features:

- Amplitude up to 1 dBm (50 Ω)
- Amplitude resolution of at least 14 bit (better 16 bit)[2]
- Frequency range of 75 MHz to 100 MHz
- Four output channels with at least two separately controllable tones per channel
- Flexible and fast way of handling a digital phase modulation control signal for active stabilization
- Phase-continuous frequency chirps over the full AOD bandwidth within 100 µs
- Amplitude ramps from zero to full power (1 dBm) within 100 µs
- Phase modulation of all tones (four channels, two tones per channel) with an update rate of at least 1 kHz (preferably faster, in case we need a higher control bandwidth)

Most items on this list are provided by almost all frequency generators. But while researching, we found that the for us crucial feature of having a digital (modulation) input that can deal with a user-defined data stream is quite rare. Fortunately, since at the time of researching the frequency source, the FPGA part of the feedback scheme has not been developed yet, we are completely flexible on the details of this communication protocol.

We will present a short summary of all the serious contenders[3] and in the end explain how we came to our conclusion of choosing the Software Defined Radio (SDR) based solution *USRP N310* from Ettus Research[4] (National Instruments).

HDAWG (Zurich Instruments)

The HDAWG of Zurich Instruments[5] is an Arbitrary Waveform generator (AWG). This means that a sequence memory is filled with waveform data before the device operation. This data is then output onto the analog channels by a sequence processor. This sequence processor also has limited capability of manipulating this data in real-time while outputting (see the QRM paragraph below for more details). The device comes in two different models, one with four and the other with eight output channels. There is a possibility to pay for a firmware upgrade which enables multiple tones per channel. The problem is that in this multiple frequency mode, only real-time control over PC-software is possible for individual tones (the sequence processor can only manipulate both tones equally). This would not be fast enough for the active stabilization. In addition to that, a feedback scheme that involves a PC with an ordinary operating system does not have a well defined bandwidth, since Ethernet communication is not deterministic. This leaves only

[1] With digital modulation there will of course always be discontinuities due to the quantization of the modulation signal. Here we mean there must be no discontinuities greater then the phase- and frequency resolution.

[2] Initially, we did not have this constraint, but after testing the DDS board with 10 bit amplitude resolution, we decided to add this point.

[3] For the standard characteristics, such as bandwidth and resolution, we refer to the manufacturers site. Here we will almost exclusively summarize information that has been gathered during direct correspondence with the manufacturers that cannot be found online.

[4] https://www.ettus.com

[5] https://www.zhinst.com

the 8 channel model or two of the four channel models as viable options, and then combining two channels externally into one AOD drive signal (synchronization of two 4 channel HDAWG is possible via a 10 MHz pulse signal). The device offers an external digital 32 bit IO port. It is possible to use the 32 bit word to invoke a specific predefined sequencer instruction (there is a total of 16000 possible sequencer instructions). In our case, we would define instructions such as 'change the phase of channel x by y'. This gives a maximum phase resolution of $2\pi/2000$ rad per channel. What also has to be kept in mind with every AWG is the limitation of the sequence memory. In order to be able to output 100 MHz we need a sample rate on the order of 1 GSa/s. The device has a sequence memory (with the memory upgrade) of 500 MSa. This leaves us only with five possible frequency chirps of 100 µs duration (frequency chirps have to be programmed explicitly into the sequence memory, since it is not possible for the sequencer to perform frequency modulation. Amplitude ramps can be done by the sequencer). Even though we are confident that we would be able to implement the features necessary for the active stabilization on this device, we have decided against it, the main reason being the limit of the sequence memory.

Qubit Control Module from QBlox

The Qubit Control Module (QCM) is another type of AWG, sold by QBlox[6]. The module itself is not for stand-alone operation, but has to be combined with the Cluster Control Module (CCM). The QCM is designed as an analog card with four output channels. The CCM can host up to 20 modules. Since the QCM is an AWG at its core, it shares many problems with the HDAWG from Zurich Instruments. The reason we considered this device in addition to the HDAWG lies in the details of the device's internal structure. A block diagram of the device can be seen in Figure 2.8. The QCM additionally has a numerical oscillator (NCO) between the sequencer and the analog output. This allows for manipulation of the waveform stored in the sequence memory before outputting that go beyond the capabilities of the sequencer in the HDAWG. Concretely, this means that we would not have to explicitly write frequency ramps into the sequence memory, but can use the NCO for that, and therefore eliminate the problem with the limited sequence memory. As can be seen in the block diagram, the NCO can also perform phase modulation (noted by the ϕ above the NCO icon in the diagram). At the moment of our research, the parameters for the NCO are hard-coded into the sequencer instructions. But in correspondence with the manufacturer we were told that a firmware upgrade is in the pipeline that would enable us to set these parameters via the digital input of the CCM, which would allow us to implement the phase feedback. This digital input is only one single bit wide. Therefore, we would have to implement a serial protocol between the FPGA and the QCM. It is not clear at the time of writing this thesis (April, 2023) what bit rate can be achieved with the QCM and CCM. The block diagram shows a total of six independent cores (sequence processor plus NCO), so in order to have four channels with two tones per channel, we would need two QCMs and externally combine two outputs into one AOD drive signal (multiple modules inserted into a CCM are synchronized by default, since the clock for the individual QCM modules is provided by the CCM). Again, similar to the HDAWG, the feedback feature can be implemented with this device. But the prospect of relying on an – at the moment of the decision making – unpublished firmware upgrade, we have decided against this device as well.

DDS Board

There are many manufacturers that offer compact, single chip solutions for Direct Digital Synthesis (DDS), such as Analog[7]. Its main feature is to output a sinusoidal signal with variable frequency and phase. The basic principle of a DDS is depicted in Figure 2.9. A phase accumulator increments its output ϕ on every rising (or falling) edge of the reference clock by an amount specified by the frequency tuning word. It resets to zero when reaching 359 or above. This means that due to the working principle, the phase resolution decreases with increasing frequency. By changing this input one can modulate the frequency of the output signal. Before converting the output angle of

[6] https://www.qblox.com
[7] https://www.analog.com

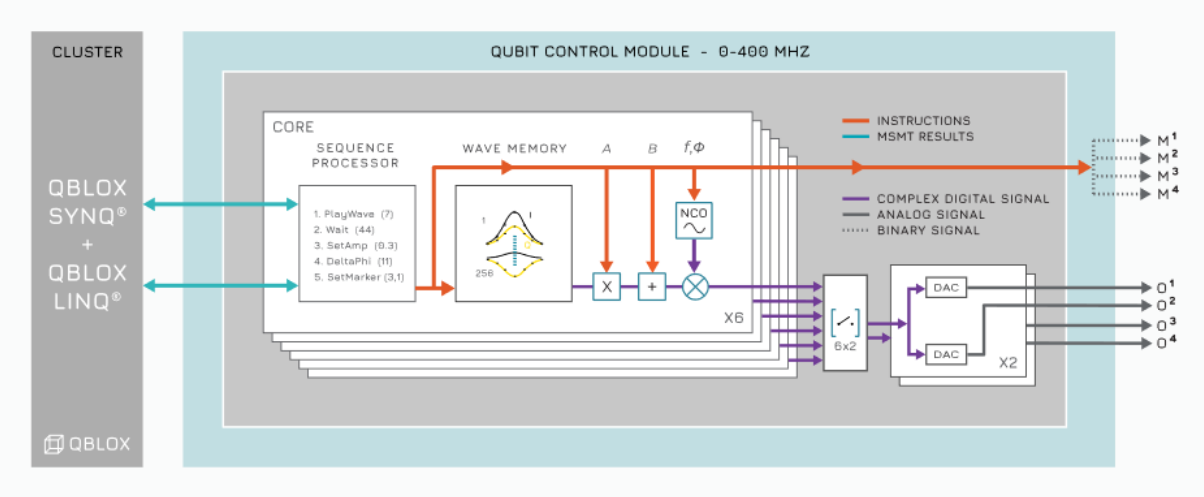

Figure 2.8: Block diagram of one of the six signal processing cores in the QRM from QBlox. The waveform stored in the wave memory can be additionally manipulated by the NCO. We would use this NCO for amplitude, frequency and phase modulation. Figure taken from [19].

the phase accumulator into a harmonic signal (denoted by $\cos\phi$ in the block diagram), there is the possibility to shift the phase by a given phase offset. This input can therefore be used to perform phase modulation.

One concrete chip we considered is the AD9959 by Analog[8]. It offers four independent output channels, so again two AD9959 would be necessary (synchronization of multiple devices is possible by supplying the same reference clock to all chips; the AD9959 offers additional synchronization features that can compensate signal propagation differences between spatially separated chips). In addition to the basic DDS features outlined above, the IC also has linear ramping capabilities for amplitude, frequency and phase. In this ramp mode, the user can specify start- and endpoint and ramp speed. Note that multiple channels can only perform the same ramp, which is sufficient for the accordion zoom-in, but might be a problem for different experimental sequences. It is also only possible to either perform amplitude, frequency or phase ramps, the chip cannot do different types of ramps at the same time. Since we need this feature for accordion lattice zoom-in, we would have to perform the amplitude ramps with external voltage controlled attenuators.

Fortunately, a host PCB for the AD9959 has already been designed by the Trapped Ion Quantum Information Group (TIQI) at ETH Zurich [20]. After testing the DDS board, we found that the 10 bit amplitude resolution of the AD9959 seems not to be good enough, and therefore updated our feature list to include an amplitude resolution of at least 14 bit. At the time of testing, we do not have a test setup for the lattice control and imaging, so we cannot say with certainty that we absolutely need this resolution. But after visually observing the output signal of the DDS, we decided to go for the 14 bit limit. Developing a host PCB board for a more powerful DDS chip would be too time consuming.

USRP Series from Ettus Research

USRP stands for Universal Software Radio Peripheral and such devices are used in the space of Software Defined Radio (SDR). The basic idea of SDR is to supply the data for radio signals (for example an audio data stream) by a software running on a PC. The hardware (i.e. the USRP) is then only used to convert the signal from digital to analog and mix it up into the radio band. This allows the user to implement most of the signal processing on the PC, which is much more flexible

[8] analog.com

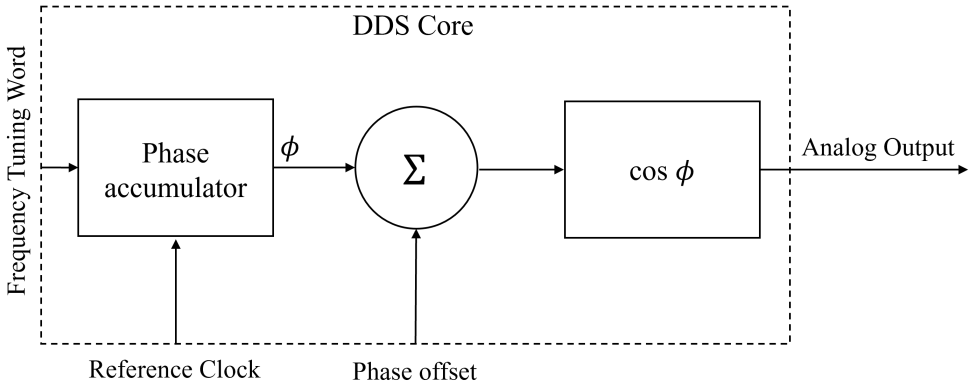

Figure 2.9: Working principle of a Direct Digital Synthesis (DDS) core. The phase accumulator increments on every edge of the reference clock by an amount specified by the frequency tuning word. A phase offset can be added to the accumulated value. The output stage calculates the cosine of the (offset) accumulated phase and performs digital to analog conversion. If the frequency tuning word and the phase offset is held constant, a pure sine-wave is outputted. By ramping the frequency tuning word, frequency modulation can be performed. Similarly, ramping the phase offset gives a phase modulated signal.

and also cheaper than the hardware implementation. All USRP devices from Ettus communicate with the PC via Ethernet and use the open source software GNU Radio[9]. USRPs are equipped with an FPGA that handles the Ethernet communication and can also be used for additional signal processing (the FPGA can be thought of as a hardware accelerator to the signal processing on the PC; more on this later). One can use predefined code blocks or even write custom FPGA firmware. The software on the PC supplies the data as a complex I/Q data stream [21]. This data is then, after the additional signal processing by the FPGA, mixed up into the desired radio band by an I/Q mixer using an internal local oscillator (LO) [21].

The devices that come into question are the USRP X310 and the USRP N310 [22]. The X310 does not have built-in mixers. These have to be installed with separately sold Daughterboards. These boards come with different specifications and have to be chosen for the application at hand. Ettus offers so called BasicTX Daughterboards [23], which simply feed through the two DAC outputs onto SMA ports (one for the I and one for the Q channel) and are intended for external mixing. In our case we would not mix at all, but use the I and Q outputs as separate channels and supply two AODs with one BasicTX board (since the generation of the I/Q data is done via software, we can add an arbitrary number of tones to one channel). We therefore rely completely on the bandwidth of the X310 DACs, which is exactly 100 MHz (sample rate of 200 MSa/s). The X310 can host two of these boards, so we can drive all four AODs with one X310 and two BasicTX Daughterboards.

The N310 does the mixing internally, so it hosts four I/Q pairs. One big advantage of the N310 over the X310 is that the four radio signal streams are synthesized on the same device, where as the X310 operates on two separate entities (one for each Daughterboard). These entities are only synchronized via a 10 MHz signal, whereas all four output channels of the N310 are sourced by the same FPGA clock.

Both devices are equipped with a serial general purpose IO port, which can be accessed by the FPGA directly. Therefore we can implement our own communication protocol with the FPGA that generates the phase control signal. Since streaming eight 100 MHz signals over Ethernet would require a very powerful PC, we plan to implement a DDS on the FPGA, which takes amplitude

[9] https://www.gnuradio.org/

Device	Price in CHF	Bandwidth	Resolution	Ramp feature	Remarks
HDAWG	50k 2x HDAWG4 with memory extension	750 MHz	16 bit	(Yes)	Feedback implementation with limited phase resolution. Sequence memory issue
QCM	36k 2x QCM, 1x CCM	400 MHz	16 bit	Yes	Feedback implementation depends on a not yet[11] published software update
DDS Board	1k	200 MHz	10 bit	(Yes)	External parts needed for ramping
X310	20k 2x X310 + BasicTX	100 MHz	16 bit	Yes	Bandwidth on lower limit
N310	18k 1x N310	100 MHz	14 bit	Yes	Bandwidth is no problem due to mixing. Very good synchronization.

Table 2.1: Comparison of the selection of possible frequency sources for driving the AODs. We found that the USRP N310 from Ettus Research fits our needs best.

and frequency information from the PC. Therefore the PC can be used to control the experimental sequence, while the signal generation is completely done on the FPGA[10]. This of course somehow defies the purpose of an SDR, but the reason these devices are so attractive for our purpose is the development environment it offers. Developing such a FPGA board ourselves would be an immense amount of work. With the USRPs we have devices that work out-of-the-box and their functionality is very flexible due to custom FPGA code.

USRP N310

From the above listing of possible devices and the summary table 2.1 it is clear that we could probably implement all necessary features with every device on that list. But by also taking price and implementation effort into consideration, we concluded that the USRP N310 from Ettus Research is the only sensible choice. Both AWG solutions are very expensive and are not really intended to be used as a device in a feedback loop. The DDS board would be a great and very cost effective alternative, but the missing ramping capabilities and low amplitude resolution of the board developed by TIQI, and the high effort of creating such a board from scratch with a more capable DDS chip, make this solution sub-optimal as well. This only leaves the USRP devices from Ettus as viable choices. Between the N310 and X310 it is also clear that, for us, the latter only has disadvantages over the former (except for the amplitude resolution), while also being more expensive. In the rest of this chapter we want to go into more detail about the functionality and how we plan to integrate this device into the feedback scheme and experimental sequence.

As we already mentioned in the device comparison, the USRP N310 is used as the hardware part of a Software Defined Radio (SDR). There, the base band data is send from a PC via Ethernet to the device, which then handles the digital-to-analog conversion and the mixing into the radio band (typically several Gigahertz). Therefore, when talking about the bandwidth of an USRP, one has to differentiate between immediate- (or base band) and total bandwidth. The former is

[10] If it turns out this is too non-deterministic, we also have the possibility of loading the sequence onto the FPGA before the experiment run.

given by the maximal output frequency of the I and Q DAC. The latter can be understood as the difference between the maximum and minimum frequency that can be output by the USRP. But this bandwidth is not accessible immediately. When choosing a LO frequency, one limits the output bandwidth to LO frequency plus/minus half of the immediate bandwidth. If one wants to output a signal with frequency outside of this range, one has to first change the LO frequency, which takes several milliseconds.

The way we intend to use the USRP, we are mostly interested in the immediate bandwidth. But there we do not need the full 100 MHz, since we mix the output of the DAC with the LO. Therefore, we only use 25 MHz bandwidth (our signals lie in between 75 MHz and 100 MHz). But still, streaming eight 25 MHz signals via Ethernet is not so simple, we will generate them on the USRP FPGA. A signal-flow diagram is shown in Figure 2.10. We will use the stream data from the PC as amplitude envelope and frequency data. Therefore, we need to intercept the IQ-stream, as shown in the orange outlined boxes. Per channel we have two tones, each with its own amplitude and frequency data. This gives a total of eight complex IQ-streams. This information is then passed to a DDS block on the FPGA, that uses this amplitude and frequency data to generate two tones. As mentioned in the DDS board comparison, a DDS also has a phase offset input. This we will use for the phase stabilization.

A FPGA block that handles the serial connection to the external FPGA and de-serializes this protocol to hand the relevant data to the different DDS blocks has to be implemented as well. In case it turns out that the Ethernet stream is not fast enough for the amplitude envelope and frequency data either, we have the possibility to implement this part on the FPGA as well and use the USRP as a stand-alone device. In that case, the amplitude and frequency data is loaded onto the FPGA before the experimental sequence, and we provide a trigger input for the different stages of the sequence. Whether this is necessary or not, we can only judge after a first implementation and testing. Due to time constraints this was not done during this thesis.

Ettus provides the user with a custom IDE called RFNoC[12] for the development and integration of user FPGA code. The software also provides already existing signal blocks, such as a DDS block. The user can then create a new block, define its input- and output signals, write the signal processing code and update the FPGA firmware. The signal flow path between different blocks is also managed within this IDE.

[12] https://www.ettus.com/sdr-software/rfnoc/

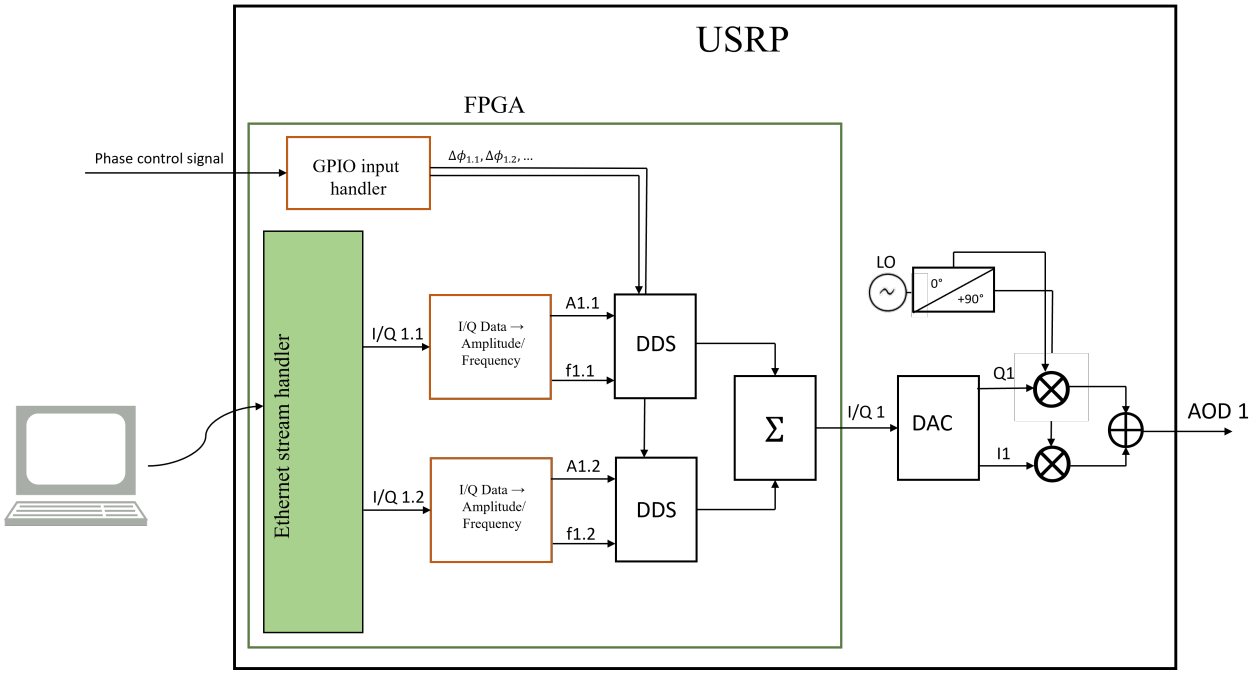

Figure 2.10: Planned implementation of the AOD frequency source with feedback capabilities using the USRP N310. The block diagram only shows one of four processing blocks. We denote a quantity for AOD output channel x and lattice i with x.i (x=1,2,3,4 and i=1,2). Blocks that are not available from the RFNoC software are boxed orange. The core piece of this implementation are the two DDS cores that create the two sinusoidal driving tones (one for each lattice) for the AOD. The amplitude and frequency information are streamed from a PC via the GNU Radio software. The two blocks with input I/Q1.i split the I/Q streams and interpret it as amplitude and frequency information. This is given to the DDS core. The GPIO input handler de-serializes the stream incoming from the external FPGA and splits it up into phase corrections for each driving tone. The sum of the output of the two DDS cores is mixed up with an LO frequency of $f = 87.5\,\mathrm{MHz}$ (center of the AOD bandwidth).

Chapter 3

Second Harmonic Generation

In order to achieve the desired lattice constants, we have to be able to supply a high power laser beams with 532 nm wavelength. Since commercial laser sources at this wavelength are hardly available for high power and also very expensive, we decided that for the new setup, we will use a frequency doubled 1064 nm commercial laser source [*Azure Light Systems* (ALS) 45 W] using second harmonic generation. Another reason for this variant is that commercial solutions often cannot be repaired in-house. This can lead to long down-times or having to buy a backup device. We will start with an overview of the theoretical description of SHG. Then we will present the setup that was developed during this thesis. At the end of the chapter we also show characterization measurements done on this setup.

3.1 Theory

Many interesting and technologically useful optical phenomena, such as the Kerr effect, parametric down-conversion and second harmonic generation (SHG), are possible only due to the nonlinear characteristics of dielectric media [15]. Mathematically speaking, this non-linearity shows up as higher order terms in the series expansion of the induced polarization density in powers of the incident electric field:

$$P_i = \epsilon_0 \chi E_i + 2dE_i^2 + 4\chi^{(3)} E_i^3 + \dots, \tag{3.1}$$

where $i = 1, 2, 3$ denoting the three spatial dimensions (we assume an isotropic and homogeneous medium if not stated otherwise). It was long thought that all optical media are linear. Only with the advancements of lasers, which gave access to much higher field strengths, nonlinear effects became observable [24]. The coefficients of the expansion are determined by the optical medium. The linear coefficient is the well-known linear susceptibility, which is related to the refractive index by $n^2 = 1 + \chi$. It is convenient to write the polarization density as the sum of a linear term and the nonlinear terms: $P = \epsilon_0 \chi E + P_{\mathrm{NL}}$. For now we will assume a dispersionless and isotropic medium. Then the wave equation governing the total electric field in the absence of free charges and currents can be written as

$$\nabla^2 E - \frac{n^2}{c^2} \frac{\partial^2 E}{\partial t^2} = -S = \mu_0 \frac{\partial^2 P_{\mathrm{NL}}}{\partial t^2}, \tag{3.2}$$

where n is the index of refraction [15]. From this one can see that the nonlinear part of P can be interpreted as a source term to the wave equation. Since P_{NL} depends non-linearly on E, this equation can only be solved approximately. One possible way of tackling this problem is the Born approximation [15]. It is an iterative approach, where the source term is initially calculated

from the incident wave, then the wave equation is solved. The result is called the first-order Born approximation. If necessary, one can proceed to higher order by again calculating the source term with this new solution and repeating the steps above.

Assume we have a plane wave $E(r,t) = E_0 \cos(kr - \omega_0 t)$ incident on a medium with only a second-order non-linearity, i.e.

$$P_{\mathrm{NL}}(E) = 2dE^2 = 2dE_0^2 \cos^2(kr - \omega_0 t) = dE_0^2 \left(1 + \cos(2kr - 2\omega_0 t)\right). \tag{3.3}$$

In the first Born approximation, this results in an electric wave oscillating at $2\omega_0$[1]. This process is called Second Harmonic Generation (SHG). From this it can already be seen that the intensity of the second harmonic depends on d^2 and $E_0^4 \propto I_0^2$, where I_0 is the intensity of the incoming wave.

As mentioned above, the prefactors in the expansion of the polarization are determined by the optical medium. This implies that symmetries of the lattice have to be respected by these macroscopic quantities. Again assume a medium with only a second order non-linearity. Spatially inverting both the medium and the incident wave changes the sign of the polarization, since the polarization has its origin from microscopic dipoles in the medium. But according to equation 3.1, for P to change sign, d must change sign. This implies that the crystal cannot posses inversion symmetry, since this would leave d invariant.

Coupled wave equations

We will now go back to the nonlinear wave equation (eq. 3.2) and treat it more formally (this sections follows closely the treatment in Ref. [15]). We write the electric field and the nonlinear part of the polarization density as a sum of monochromatic modes

$$\begin{aligned} E(\mathbf{r},t) &= \sum_n E^{(n)}(\mathbf{r},t) \\ P_{\mathrm{NL}}(\mathbf{r},t) &= \sum_n P_{\mathrm{NL}}^{(n)}(\mathbf{r},t), \end{aligned} \tag{3.4}$$

where each mode is written as

$$\begin{aligned} E^{(n)}(\mathbf{r},t) &= E^{(n)}(\mathbf{r})e^{-i\omega_n t} + \text{c.c.} \\ P_{\mathrm{NL}}^{(n)}(\mathbf{r},t) &= P_{\mathrm{NL}}^{(n)}(\mathbf{r})e^{-i\omega_n t} + \text{c.c.} \end{aligned} \tag{3.5}$$

Here we assume a lossless and isotropic medium, which is why we can write the field as a scalar quantity. Substituting into the wave equation, every mode has to fulfill

$$\nabla^2 E^{(n)}(\mathbf{r}) + \frac{\omega_n^2 n^2(\omega_n)}{c^2} E^{(n)}(\mathbf{r}) = -\frac{\omega_n^2}{\epsilon_0 c^2} P_{\mathrm{NL}}^{(n)}(\mathbf{r}). \tag{3.6}$$

For SHG, we know that there are two modes present: the fundamental wave at $\omega_1 = \omega$ and the second harmonic at $\omega_2 = 2\omega$. Note that since we assume frequency independent nonlinear parameters, the presence of the modes with frequencies ω and 2ω allows processes that lead to even higher harmonics, but as we will see later, these processes are highly suppressed. We assume the plane waves describing a single mode propagates in z-direction. Furthermore, we separate the amplitude of every mode into a fast and slowly oscillating component:

$$E^{(n)}(z) = A_n(z)e^{ik_n z}, \tag{3.7}$$

where $k_n = \frac{n(\omega_n)\omega_n}{c}$. The total electric field and the nonlinear polarization density are therefore given by

$$\begin{aligned} E(z,t) &= A_1(z)e^{ik_1 z - i\omega t} + A_2(z)e^{ik_2 z - i2\omega t} + \text{c.c.} \\ P_{\mathrm{NL}}(z,t) &= P_1(z)e^{-i\omega t} + P_2(z)e^{-i2\omega t} + \text{c.c.} \end{aligned} \tag{3.8}$$

[1] The constant term in P_{NL} gives rise to another nonlinear effect, called optical rectification.

Note that the space dependent amplitudes of the nonlinear polarization density $P_n(z)$ are not separated into slow and fast oscillating terms. In order to find expressions for these two terms, one has to investigate equation 3.1 to see which products of electric field modes lead to the corresponding frequencies in the nonlinear polarization density. It is hence obvious that

$$\begin{aligned} P_1(z) &= 4\epsilon_0 d E_2 E_1^* = 4\epsilon_0 d A_2 A_1^* e^{i(k_2-k_1)z} + \text{c.c.} \quad \text{and} \\ P_2(z) &= 2\epsilon_0 d E_1^2 = 2\epsilon_0 d A_1^2 e^{i2k_1 z} + \text{c.c.} \end{aligned} \tag{3.9}$$

Inserting all of these expressions into the wave equation and applying the slowly-varying amplitude approximation (i.e. ignoring the terms $\frac{\mathrm{d}^2 A_n}{\mathrm{d}z^2}$) we find the two equations

$$\begin{aligned} \frac{\mathrm{d}A_1}{\mathrm{d}z} &= \frac{2i\omega_1^2 d}{k_1 c^2} A_2 A_1^* e^{-i\Delta k z} \\ \frac{\mathrm{d}A_2}{\mathrm{d}z} &= \frac{i\omega_2^2 d}{k_2 c^2} A_1^2 e^{i\Delta k z}, \end{aligned} \tag{3.10}$$

relating the amplitude of the fundamental and second harmonic wave, where $\Delta k = 2k_1 - k_2$ is the so called phase mismatch. The derivative of the second harmonic intensity with respect to z is given by

$$\frac{\mathrm{d}I_2}{\mathrm{d}z} = 2n_2\epsilon_0 c \left(\frac{\mathrm{d}A_2}{\mathrm{d}z} A_2^* + A_2 \frac{\mathrm{d}A_2^*}{\mathrm{d}z} \right) = \frac{2n_2\epsilon_0\omega_2^2 d}{k_2 c} \left(A_1^2 A_2^* \frac{e^{i\Delta k z}}{\Delta k} + \text{c.c.} \right) \tag{3.11}$$

Using a similar expression for $\frac{\mathrm{d}I_1}{\mathrm{d}z}$, one can immediately see that

$$\frac{\mathrm{d}I_1}{\mathrm{d}z} = -\frac{\mathrm{d}I_2}{\mathrm{d}z}. \tag{3.12}$$

This is of course not surprising, but it will be useful later on.

For the sake of completeness, we will also mention the *undepleted-pump approximation*, where one assumes a constant fundamental field $A_1(z) = \text{const}$. Then equation 3.10 can simply be integrated and the intensity of the second harmonic after a nonlinear slab of length L is given by

$$I_2(L) = 2n_2\epsilon_0 c |A_2(L)|^2 = \frac{8d^2 w^2 I_1^2}{n_1^2 n_2 \epsilon_0 c^3} L^2 \mathrm{sinc}\left(\frac{\Delta k L}{2}\right), \tag{3.13}$$

assuming no second harmonic is present at the input of the slab. From this expression we can already see that, in order to have the highest conversion efficiency, we have to meet the *phase matching condition*, $\Delta k = 0$. But, since efficiencies of 30 % and more are achievable with SHG, this approximation is not overly useful. Armstrong *et al.* have solved the full coupled equations in the slowly varying amplitude approximation [24]. Here we will only show the main results.

Exact solution to the coupled wave equations

In order to solve the coupled equations describing SHG, given by

$$\begin{aligned} \frac{\mathrm{d}A_1}{\mathrm{d}z} &= \frac{2i\omega_1^2 d}{k_1 c^2} A_2 A_1^* e^{-i\Delta k z} \\ \frac{\mathrm{d}A_2}{\mathrm{d}z} &= \frac{i\omega_2^2 d}{k_2 c^2} A_1^2 e^{i\Delta k z}, \end{aligned} \tag{3.14}$$

Armstrong *et al.* introduce the following substitutions:

$$\begin{aligned} A_1(z) &= \left(\frac{I_1+I_2}{2n_1\epsilon_0 c}\right)^{1/2} u_1(z)e^{i\phi_1(z)} \quad \text{with} \quad u_1, \phi_1 \in \mathbb{R} \\ A_2(z) &= \left(\frac{I_1+I_2}{2n_2\epsilon_0 c}\right)^{1/2} u_2(z)e^{i\phi_2(z)} \quad \text{with} \quad u_2, \phi_2 \in \mathbb{R} \\ \xi &= z/l \quad \text{where} \quad l = \left(\frac{n_1^2 n\epsilon_0 c}{2(I_1+I_2)}\right)^{1/2} \frac{c}{\omega_1 d} \\ \theta &= 2\phi_1 - \phi_2 + \Delta k z \\ \Delta s &= \Delta k l \end{aligned} \tag{3.15}$$

The definitions for $u_{1(2)}$ and $\phi_{1(2)}$ allow to write the equations in terms of one phase variable θ. The variable ξ expresses distance in terms of the characteristic length scale l over which the fundamental and second harmonic exchange energy. Also note that $I_1 + I_2$ is constant due to equation 3.12. Substituting these expressions into the coupled wave equations gives

$$\begin{aligned} \frac{\mathrm{d}u_1}{\mathrm{d}\xi} &= u_1 u_2 \sin\theta \\ \frac{\mathrm{d}u_2}{\mathrm{d}\xi} &= -u_1^2 \sin\theta \\ \frac{\mathrm{d}\theta}{\mathrm{d}\xi} &= \Delta s + \frac{\cos\theta}{\sin\theta}\frac{\mathrm{d}}{\mathrm{d}\xi}(\ln u_1^2 u_2). \end{aligned} \tag{3.16}$$

As a first observation we notice from the second equation that, whether the intensity of the second harmonic decreases or increases with z, depends on the sign of $\sin\theta$.

In the case of perfect phase matching (i.e. $\Delta s = 0$), the three equations can be solved by noticing that the third equation is equivalent to $\frac{\mathrm{d}}{\mathrm{d}\xi}\ln\left(\cos\theta u_1^2 u_2\right) = 0$. Hence the quantity $\Gamma = \cos\theta u_1^2 u_2$ is constant and can be used to decouple the three equations. The general solution can be written in terms of Jacobi elliptic functions, but becomes particularly simple in the case of $\Gamma = 0$. Since Γ is a conserved quantity, it can be found via the initial conditions at the beginning of the nonlinear medium. The condition $\Gamma = 0$ implies that either one of the two input fields is zero or their initial phase allows for $\cos\theta = 0$. In this special case, the solutions are given by

$$\begin{aligned} u_2(\xi) &= \tanh(\xi + \xi_0) \\ u_1(\xi) &= 1 - u_1^2(\xi) \end{aligned} \tag{3.17}$$

where ξ_0 is determined by initial conditions. The second equality is a direct consequence of equation 3.12. The amplitudes u_1 and u_2 are plotted for the initial conditions $u_1(0) = 1$ and $u_2(0) = 0$ in Figure 3.1(a). One sees that, in these ideal conditions [(perfect phase matching, no absorption and thermal effects (see following section)] with a sufficiently long crystal, arbitrary conversion efficiencies can be achieved. The more general case, where both the fundamental and the second harmonic are present at the entrance face of the medium with relative phases such that $\Gamma \neq 0$, is shown graphically in Figure 3.1(b). There one can see that the fundamental and the second harmonic exchange power periodically and the highest achievable efficiency is far from one. This is an important result for multi-crystal arrangements (more on that in the next section).

In case the phase matching condition is not met (i.e. $\Delta s, \Delta k \neq 0$), the solution to equation 3.16 can also be written in terms of Jacobi elliptic functions, but we will only show the solution of the second harmonic field amplitude graphically in Figure 3.2. There we see that, for finite phase mismatch, the amplitude of the second harmonic field also oscillates, but has a smaller maximum and goes completely to zero at certain points in the medium. We also see that the oscillation period depends on the phase mismatch.

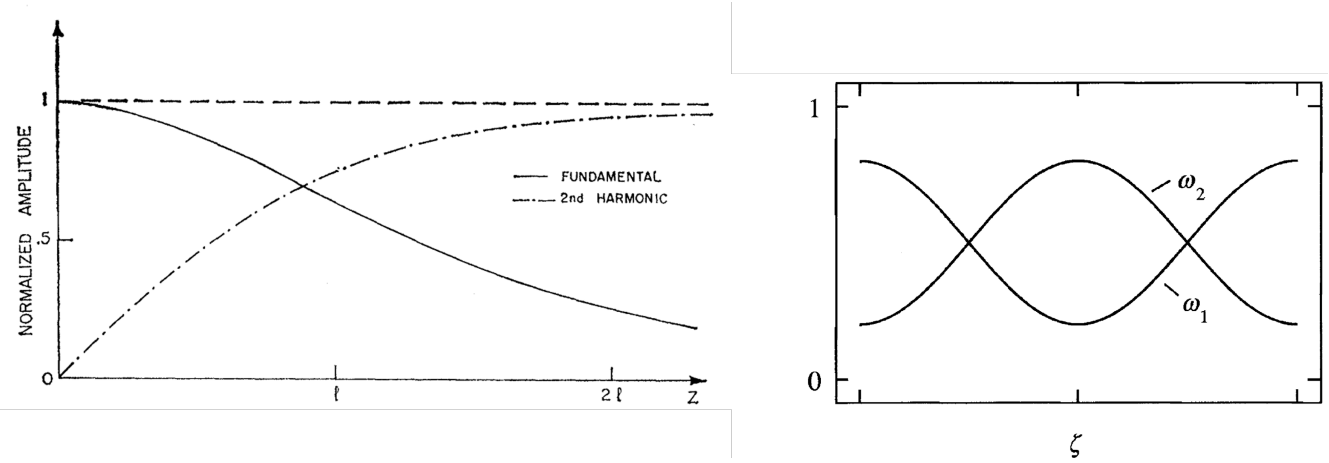

Figure 3.1: (a) Intensity of the fundamental and second harmonic as a function of distance ($z = 0$ denotes input face of crystal) for perfect phase matching with no second harmonic present at $z = 0$. The conversion efficiency goes to 1 for $z \to \infty$. (b) Intensity of the fundamental and second harmonic as a function of normalized distance with perfect phase matching and second harmonic light present at the input. In the situation shown here, the phase of the two waves at the input do not fulfill $\Gamma = 0$. Therefore, the fundamental and second harmonic exchange energy periodically.

Phase matching and quasi phase matching

In the previous section we have seen that, in order to achieve maximal conversion efficiency, the phase matching condition

$$\Delta k = 2k_1 - k_2 = 0 \iff \frac{2\omega}{c}(n_1 - n_2) = 0, \tag{3.18}$$

has to be met. As a reminder, n_1 and n_2 is the refractive index at the fundamental and second harmonic frequency, respectively. Up until now, we have treated our nonlinear medium as isotropic. For the following discussion, we have to consider the polarization dependence of the refractive index (i.e. bi-refringence) and the nonlinear second order susceptibility. This leads to an expansion of the i-th component of the polarization density of the form[2] (using Einstein summation)

$$P_i(\omega_j, \omega_k) = \epsilon_0 \chi_{ij}(\omega_j) E_j(\omega_j) + 2 d_{ijk} E_j(\omega_j) E_k(\omega_k) + \ldots, \tag{3.19}$$

where $i, j, k = 1, 2, 3$ denote the three principal axis of the crystal and χ and d are now tensors of rank 2 and 3, respectively. In our case, $E_j = E_k$ and $\omega_j = \omega_k$. Due to crystal symmetries one can map the three indices i, j, k to two indices i, l, where the correspondence is given by [15]

jk	11	22	33	23, 32	31, 13	12, 21
l	1	2	3	4	5	6

(3.20)

The medium we are using for SHG, and almost all others available, exhibit a strong polarization dependence of the second order non-linearity. For the material in use in this project, $MgO : LiTaO_3$, the second order nonlinear coefficients relevant for SHG are $d_{33} = 13.8\,\mathrm{pm\,V^{-1}}$ and $d_{31} = 0.85\,\mathrm{pm\,V^{-1}}$.

There are multiple ways of achieving phase matching. Most of the time though, only one or none of these techniques is compatible with the material properties. The first possibility is to use the

[2]Here we do not give the full frequency dependence of the second order non-linearity, since it is not important for us. The frequency dependence of the linear susceptibility is of course vital in the context of phase matching.

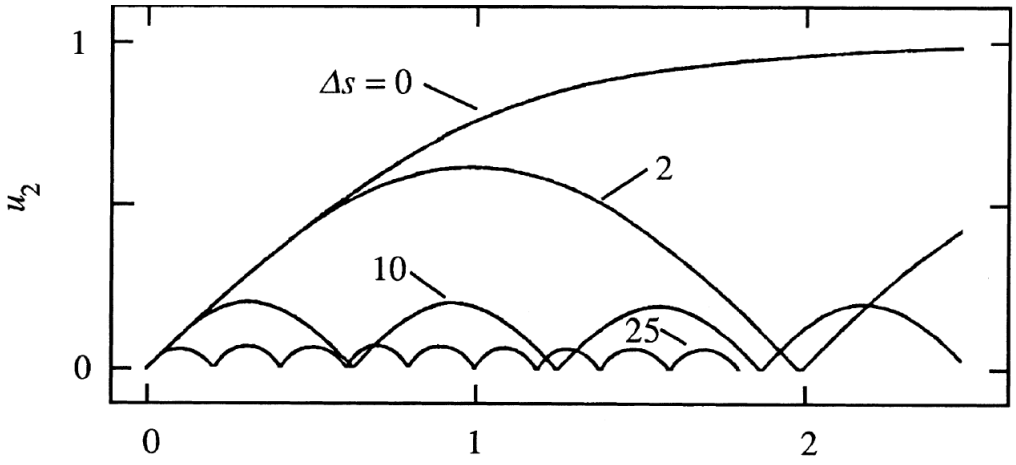

Figure 3.2: Intensity of the second harmonic as a function of distance for various values of $\Delta s = \Delta k l$ with no second harmonic present at the input facet. For perfect phase matching ($\Delta s = 0$), the intensity monotonically increases with distance in the crystal. When the phase matching condition is violated ($\Delta s \neq 0$), the intensity oscillates, but never exceeds a certain value given by the amount of phase mismatch.

temperature and polarization dependence of $n_{i,e(o)} = n(\omega_i, T, \mathbf{e}_{e(o)})$ in order to achieve $n_{1,e(o)}(T) = n_{2,e(o)}(T)$, where T is the temperature and $\mathbf{e}_{e(o)}$ denotes polarization along the (extra-)ordinary axis. Whether or not this is possible for a given material depends on the exact temperature dependence of the index of refraction for a certain set of polarizations. For most materials, n is a decreasing function of wavelength, no matter the temperature. So in most cases, temperature phase matching with the fundamental and second harmonic having the same polarization (also called type 0 phase matching) is not possible. As an example, we plot the refractive index of the nonlinear crystal used in this project ($MgO : LiTaO_3$) as a function of wavelength for the ordinary- and extraordinary axis in Figure 3.3. From this we see that in the accessible temperature range in the lab (20 °C to 70 °C), temperature phase matching is not possible for the given material.

The next possibility is to use angle tuned phase matching. This technique uses the polarization angle dependence of the refractive index in a birefringent material, which is given by

$$\frac{1}{n^2(\theta)} = \frac{\sin^2\theta}{n_o^2} + \frac{\cos^2\theta}{n_e^2}, \tag{3.21}$$

where θ is the angle between the extraordinary axis and the wavevector [17]. From this equation one can see that the birefringence has to be at least as large as the dispersion in order to be able to achieve phase matching (i.e. $n_1(\theta) = n_{2,e(o)}$ or $n_{1,e(o)} = n_2(\theta)$). The angle tuning of the refractive index is plotted in Figure 3.4 for the crystal we will use for SHG. This shows that angle phase matching is not an option, either.

A more advanced phase matching technique is called *Quasi Phase matching* (QPM). First of all, we define another length scale, called the coherence length

$$L_{\text{coh}} = 2\pi/\Delta k, \tag{3.22}$$

which roughly gives half the period of oscillation of the second harmonic power for finite phase mismatch (this is exact in the undepleted pump approximation). The idea is that one allows a certain amount of phase mismatch that can be achieved with a given material and tries to compensate its effect. In order to explain this approach in detail, we have to go back to equations

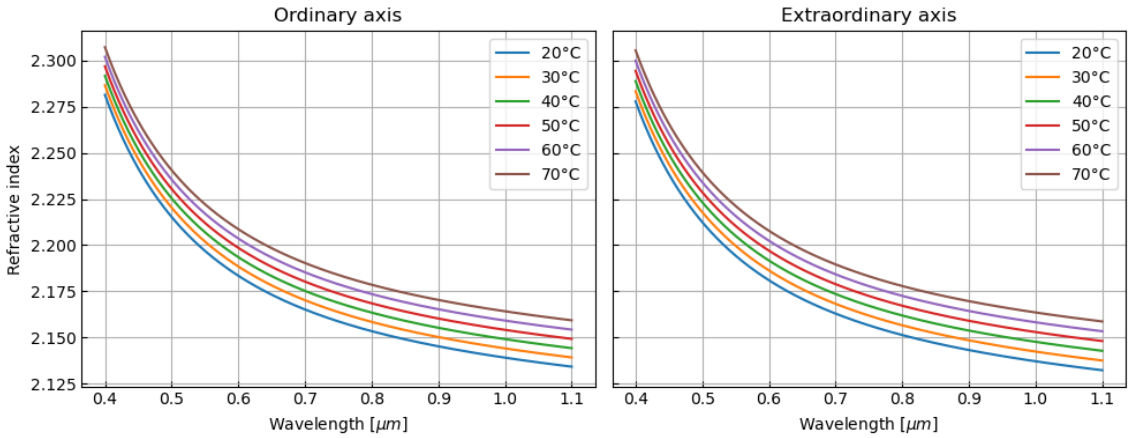

Figure 3.3: Calculated refractive index of 5 % MgO:sPPLT along the ordinary and extraordinary axis as a function of wavelength for different temperatures using the Sellmeier equation (parameters taken from Ref. [25]). We see that for the temperature range accessible to us (room temperature up to 70 °C), the refractive index for both the ordinary and extraordinary axis changes by less than 0.06 %, while the change in refractive index due to dispersion is 3.2 % (between 1.064 µm and 0.532 µm).

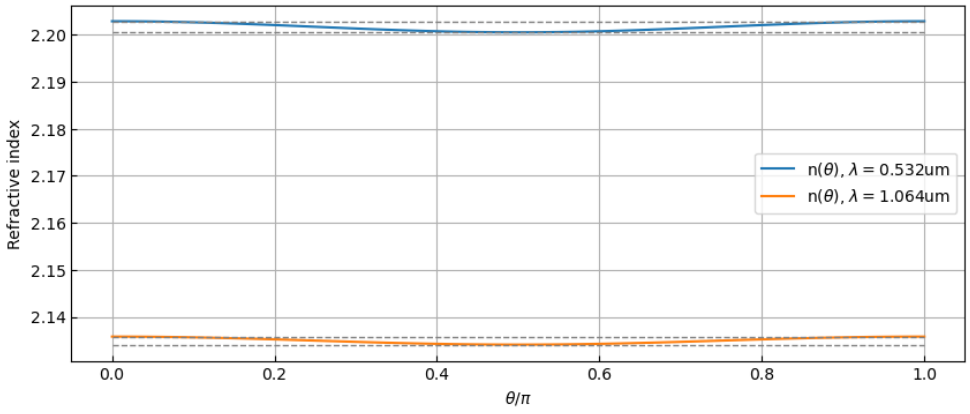

Figure 3.4: Comparison between the amount of birefringence and dispersion for 5 % MgO:sPPLT. From this we see that birefringence is not enough to achieve phase matching.

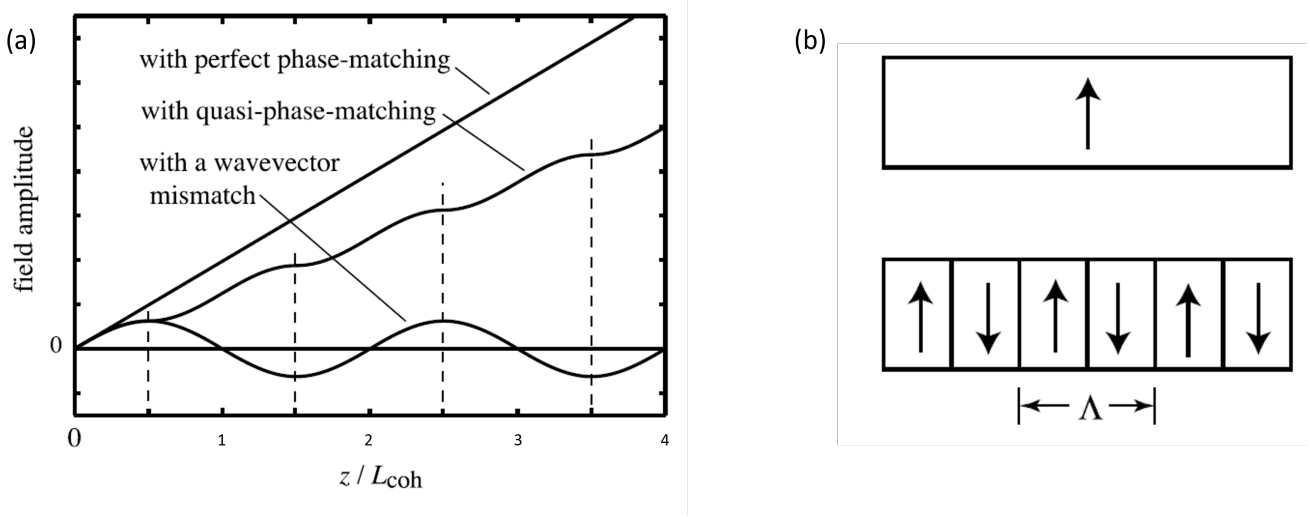

Figure 3.5: (a) Second harmonic field amplitude as a function of distance for perfect phase matching, quasi phase matching and with finite phase mismatch. In quasi phase matching, the sign of the second order non-linearity is changed at the point where the amplitude would start to decrease for a given amount of phase mismatch. (b) Sign of the second order non-linearity (indicated by arrow direction) for a crystal used in critical phase matching (top) and quasi phase matching (bottom). The period Λ with which the second order non-linearity changes sign is called poling period.

3.10. We see that we can reverse the 'direction' of power flow by flipping the sign of the second order non-linearity d. So by flipping the sign of the second order non-linearity exactly at the points in the medium where the intensity in the second harmonic would start to decrease, due to the finite phase mismatch, the second harmonic power will keep increasing further. This is depicted graphically in Figure 3.5(a). The points at which the direction of power flow is reversed are indicated with dashed lines. The period of modulation of the second order non-linearity is called *poling period* and is often denoted by Λ. This sign flip can be achieved by inverting one of the crystal axis, or by a strong, spatially alternating electric field during crystal growth [15]. The quasi phase matching technique is not as ideal as true phase matching, since the finite phase mismatch decreases the maximal attainable efficiency. But for many materials it is not possible to use angle- or temperature tuning. QPM also has the advantage that, by choosing an appropriate poling period, one can make use of the polarization that yields the highest second order nonlinear coefficient. Since the intensity of the second harmonic increases as the square of d, QPM sometimes even achieves higher efficiencies than true phase matching with a polarization with lower coupling constant.

Mathematically, QPM is best described in a Fourier picture. We replace the second order nonlinear coefficient d in the nonlinear wave equation 3.2 by a periodic, z-dependent function $d(z) = d(z+\Lambda)$, where Λ is the poling period. This function can be written as a Fourier series. We choose the form

$$d(z) = d\sum_m G_m e^{ik_m z}, \quad G_m = \frac{1}{\Lambda d}\int_0^\Lambda d(z)e^{-ik_m z}dz \quad \text{and} \quad k_m = 2\pi m/\Lambda, \tag{3.23}$$

where d is the magnitude of the second order nonlinear coefficient in the homogeneous medium. Plugging this into the nonlinear wave equation and assuming that only one Fourier component will lead to relevant coupling of the interacting waves, one arrives at the coupled equations

$$\begin{aligned}\frac{\mathrm{d}A_1}{\mathrm{d}z} &= \frac{2i\omega_1^2 d_m}{k_1 c^2} A_2 A_1^* e^{-i(\Delta k_m - 2k_m)z} \\ \frac{\mathrm{d}A_2}{\mathrm{d}z} &= \frac{i\omega_2^2 d_m}{k_2 c^2} A_1^2 e^{i\Delta k_m z},\end{aligned} \tag{3.24}$$

where $\Delta k_m = 2k_1 - k_2 + k_m$ and $d_m = dG_m$ for some $m \in \mathbb{Z}$. These equations are equivalent to the coupled equations 3.10 upon a redefinition of the phase mismatch and the nonlinear coupling constant. The modulation that is most often (almost exclusively) implemented is the one where d simply changes sign every Λ, i.e.

$$d(z) = d \operatorname{sgn}\left(\sin \frac{2\pi}{\Lambda} z\right), \tag{3.25}$$

where sgn is the signum function. Then the Fourier coefficients are given by

$$G_m = \begin{cases} \frac{2}{i\pi m}, & \text{if } m \text{ odd} \\ 0, & \text{otherwise} \end{cases} \tag{3.26}$$

Therefore, it is best to try to achieve phase matching with first order QPM, i.e. $m = 1$, since the effective coupling $|d_m|$ decreases with increasing m. Similar to true phase matching, m-th order QPM is achieved when

$$\Delta k_m = 0 \iff \Lambda = \frac{2\pi m}{k_2 - 2k_1}. \tag{3.27}$$

In this section we have summarized the theoretical treatment of SHG. We have seen that it is of vital importance to meet the phase matching condition for the material at hand, in order to achieve high conversion efficiencies. As it was described in this section, one would fix an achievable phase mismatch and look for a crystal fabricated with the right poling period. In practice, one often only has a limited selection of poling periods. So one has to find the one closest compatible to the phase mismatch at, e.g., room temperature, and then calculate the required temperature in order to achieve exact quasi phase matching. In the next section we will discuss how this is implemented in practice.

3.2 Design considerations

Before we can continue with the design of the SHG setup, we have to go back to one of the very first assumptions made in the theoretical treatment of SHG. Up until now we have assumed that the fundamental and the second harmonic field are plane waves. In reality, the fundamental beam is supplied by a laser and hence is Gaussian beam. We will not show the theoretical treatment of SHG with Gaussian beams in detail, but only summarize the practically important results. Using a Gaussian beam as the fundamental field (from now on also called pump field or pump laser) adds two more parameters that need to be optimized: the waist radius and the waist position within the nonlinear crystal. Also the (quasi) phase matching condition is modified slightly. It is not possible to solve the nonlinear wave equation using a Gaussian beam as the pump field without the undepleted pump approximation [24]. We assume that the optimal parameters that are calculated within this approximation also yield the best results in efficiency for higher pump power, where the efficiency, and hence also the pump depletion, is expected to be higher.

Gaussian beams in SHG

SHG with Gaussian beams in the undepleted pump approximation has been solved by Boyd and Kleinman (BK) [26]. They introduced the dimensionless parameters[3]

$$\xi = \frac{L}{2z_R}, \qquad \sigma = \Delta k z_R, \qquad \text{and} \quad \mu = x_0/L, \tag{3.28}$$

[3]Here we omit an additional parameter related to the spatial walk-off, since in our case we will use type zero phase matching and hence do not have spatial walk-off.

where L is the length of the crystal, z_R is the Rayleigh range of the pump beam and x_0 is the waist position within the crystal ($x_0 = 0$ refers to the center). Note that the parameter ξ is not related to the ξ used in the previous section. Boyd and Kleinman found that SHG is optimized if the parameters take on the values

$$\xi_{\text{opt}} = 2.84, \qquad \sigma_{\text{opt}} = 0.56 \quad \text{and} \quad \mu_{\text{opt}} = 0. \tag{3.29}$$

This already fixes the waist position to the center of the crystal. The other two parameters, z_R and Δk, depend on the length of the crystal. As BK point out, it is not necessary to exactly know the value of σ_{opt}, and hence Δk, since in the experiment this can be fine-tuned by changing the temperature or the crystal orientation. But knowing what ranges of Δk can be covered with the achievable temperatures helps with the design of the SHG setup.

If $x_0 = 0$, the SHG efficiency η is given by

$$\eta = \frac{P_2}{P_1} = h(\xi, \sigma) \left(\frac{16\pi^2 d^2}{n_1 n_2 c \epsilon_0 \lambda_1^3} \right) L P_1, \tag{3.30}$$

where $h(\xi_{\text{opt}}, \sigma_{\text{opt}}) = 1.068$ and P_1 and P_2 is the power of the pump and second harmonic beam, respectively.

Crystal length

The length of the crystal influences both the beam waist and the phase matching condition:

$$\Delta k = \sigma_{\text{opt}}/z_R = 2\sigma_{\text{opt}}\xi_{\text{opt}}/L \quad \text{and} \quad w_0 = \sqrt{\frac{L\lambda_1}{\pi n_1 2\xi_{\text{opt}}}}. \tag{3.31}$$

As for efficiency, the longer the crystal, the better. But a longer crystal will also be more susceptible to damage due to a temperature gradient. This has to be taken into account, since at high power, the temperature gradient due to the Gaussian beam shape (higher intensity and hence more absorption in the crystal center) can be enough to break the crystal [26]. In practice, the most common crystal lengths are $L = 10\,\text{mm}$ to $40\,\text{mm}$. If higher efficiencies are needed than what is achievable with these crystal lengths, there is also the possibility of using a multi crystal arrangement, where the output light of the first crystal (i.e. depleted pump and second harmonic) is focused again into a second crystal. As we have seen in the theory section, this complicates the setup tremendously, since the relative phase between the second harmonic and the pump field in the second crystal have to be adjusted in order to meet the phase matching condition. Here we will only use a single crystal setup.

Nonlinear material and thermal effects

There are mainly two possible choices of materials for single-pass SHG with a periodically poled crystal (for the wavelengths involved in our project, there is no material available with which one can achieve type 0 or 1 phase matching without a periodically poled crystal). One is MgO-doped Lithium Niobate (MgO:PPLN) and the other is MgO-doped Lithium Tantalate (MgO:PPLT), where the PP stands for periodically poled. The doping is used to increases resilience of the material against permanent damage due to photorefractive effects and to increase heat conductivity [27]. From now we will refer to them as PPLN and PPLT. There are two key differences between the two choices. First, PPLN has a higher second order nonlinear coefficient ($d_{33} \approx 25\,\text{pm/V}$ for PPLN and $d_{33} \approx 14\,\text{pm/V}$ for PPLT. The exact values depend on the doping concentration) [28]. Second, PPLT has a higher thermal conductivity than PPLN ($8.4\,\text{W/mK}$ for PPLT and $3.9\,\text{W/mK}$ for PPLN) [28]. Which one to choose depends on the required power output. In a realistic setup, achievable SHG efficiency gain is on the order of $1\,\%/\text{W}$ to $3\,\%/\text{W}$ for low input power (up to $\sim$5 W input power, i.e. up to 500 mW of output power) [29]. If more output power is necessary, one has to

take absorptive-, and hence thermal, effects into account. Due to the Gaussian beam shape, there is a transversal and a longitudinal thermal gradient. The associated effects are called thermal lensing and thermal dephasing, respectively [26]. Thermal lensing reduces the efficiency, but can also lead to permanent damage. This effect comes about due to the temperature dependence of the refractive index. In both materials, the refractive index increases with temperature (see Fig. 3.3 for PPLT). Since the waist of a Gaussian beam decreases with increasing refractive index, the optimal focusing condition, $\sigma = \sigma_{\text{opt}} = 0.56$, is violated and the SHG efficiency decreases, or in the worst case the tighter focus damages the material. Thermal dephasing describes the decrease in efficiency due to the thermally induced wavevector mismatch, which also stems from the temperature dependence of the refractive index. Higher thermal conductivity helps to reduce these effects. As can be seen in the Results section (Sec. 3.5), at very high input power (∼30 W) one can actually achieve higher efficiencies by loosening the focus condition and sacrificing efficiency at lower input power, in order to further decrease thermal effects.

Experimental parameters

For the experiment we will need ∼ 12 W of second harmonic power. The crystal supplier Oxide[4] suggested the use of a 30 mm long 5 % MgO:sPPLT[5] with a poling period of $\Lambda = 7.98$. The properties of our PPLT crystal relevant for SHG are compiled in table 3.1. To model the temperature and wavelength dependence of the refractive index, we use the Sellmeier equation in the form [25]

$$n^2(\lambda, T) = A + \frac{B + p(T,b)}{\lambda^2 - (C + p(T,c))^2} + \frac{E + p(T,e)}{\lambda^2 - (F + p(T,f))^2} + D\lambda^2, \tag{3.32}$$

where λ is the wavelength in micrometer and T the temperature in °C and

$$p(T,x) = x \cdot (T + 273.15)^2 \times 10^{-8}. \tag{3.33}$$

Parameters for the Sellmeier equation are from Ref. [25].

As the length of the crystal and the poling period are now known, we can calculate the temperature at which the phase matching condition is satisfied and the optimal beam waist. From the previous section, we know that the wavevector mismatch should satisfy the relation

$$\sigma = \Delta k z_R \quad \text{and} \quad \xi = \frac{L}{2z_R} \implies \Delta k = \frac{2\sigma\xi}{L} \stackrel{!}{=} \frac{2 \times 0.56 \times 2.84}{L} = 1.06 \times 10^{-4}\,\text{µm}^{-1}. \tag{3.34}$$

This imposes the condition

$$\frac{2\pi}{\lambda_1} 2(n_2(T) - n_1(T)) - \frac{2\pi}{\Lambda} - 1.06 \times 10^{-4}\,\text{µm}^{-1} \stackrel{!}{=} 0, \tag{3.35}$$

where we have set the order of quasi phase matching to $m = 1$. The temperature at which this condition is satisfied can be found numerically using the Sellmeier equation and the parameters for the extraordinary axis given in table 3.1 (the QPM condition could not be satisfied with the refractive index of the ordinary axis). The resulting quasi phase matching temperature (QPMT) is

$$T_{\text{QPM}} = 51.02\,°\text{C}, \tag{3.36}$$

as can be seen in Figure 3.6(a). Knowledge of the QPMT allows us to also calculate the optimal beam waist w_0. We again use the results from the previous section and $z_R = \frac{\pi n_1 w_0^2}{\lambda_1}$ to find

$$z_R = \frac{2\xi}{L} \stackrel{!}{=} \frac{2 \times 2.84}{L} \implies w_0 = \sqrt{\frac{\lambda_1 L}{\pi n_1(T_{\text{QPM}}) \times 5.68}} = 29\,\text{µm}, \tag{3.37}$$

[4] https://www.opt-oxide.com/

[5] The s in sPPLT stands for stoichiometric and refers to the doping technique. There are also congruent crystals, but they suffer from higher GRIIRA [27].

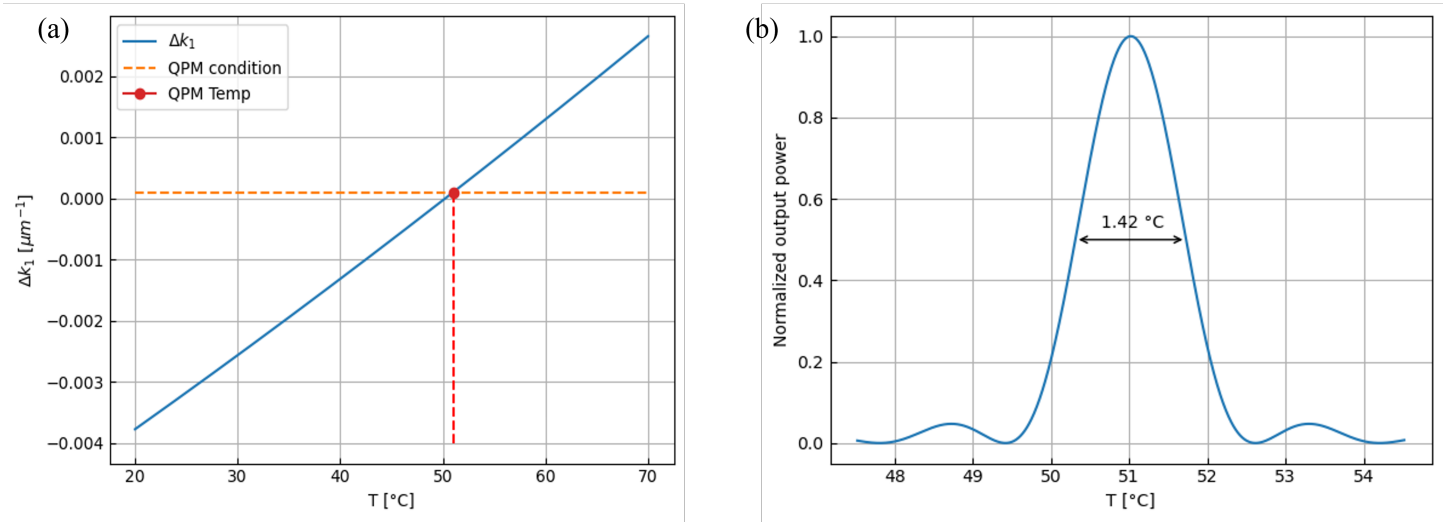

Figure 3.6: (a) Numerical calculation of the phase matching temperature. We find $T_{QPM} = 51.04\,°\mathrm{C}$. The experimental value we found for QPMT is 41 °C. (b) Calculated temperature bandwidth in the undepleted-pump approximation.

	Variable	Value
Material		5 %MgO:sPPLT
Crystal length	L	30 mm
Nonlinear coefficient [28]	d_{33}	13.8 pm/V
Poling period	Λ	7.98 µm

Table 3.1: Parameters of the nonlinear crystal (5 % MgO:sPPLT).

where $n_1(T_{\mathrm{QPM}}) = n(\lambda_1, T_{\mathrm{QPM}}) \approx 2.135$. We can also calculate a temperature bandwidth by using the results from the theory section. In the undepleted pump approximation (using QPM with Gaussian beams), we expect the phase matching factor to be of the form

$$I_2 \propto \mathrm{sinc}^2(\Delta kL) = \mathrm{sinc}^2\left(\frac{4\pi L}{\lambda_1}(n_2(T) - n_1(T)) - \frac{2\pi L}{\Lambda} - 2\xi_{\mathrm{opt}}\sigma_{\mathrm{opt}}\right). \tag{3.38}$$

From this we calculate a full-width half-maximum temperature range of $T_{\mathrm{FWHM}} = 1.4\,°\mathrm{C}$. A plot of the phase matching factor in the undepleted pump approximation as a function of temperature can be seen in Figure 3.6(b). This qualitative picture shows that it is important to keep the temperature of the crystal as constant as possible, in order to achieve stable output power. Also finding the exact QPMT improves this stability.

3.3 Experimental Setup

In the previous section we have calculated the experimental parameters we have to establish, in order to have efficient SHG. In summary, we have to make sure that the beam waist is at the center of the crystal, the beam has a waist of $w_0 = 29\,\mu\mathrm{m}$ and that the temperature of the crystal is held constant at $T_{\mathrm{QPM}} = 51.02\,°\mathrm{C}$. We will note here that the temperature at which we achieved the highest SHG efficiency does not agree with the calculated QPMT. We found experimentally

$$\tilde{T}_{\mathrm{QPM}} = 40.45\,°\mathrm{C}. \tag{3.39}$$

We will elaborate more on this in the Results section. We use a Peltier element to keep the crystal temperature at a constant value. The Peltier element with the crystal housing with included temperature sensor (NTC10k) we used is the standard temperature control scheme supplied by Oxide

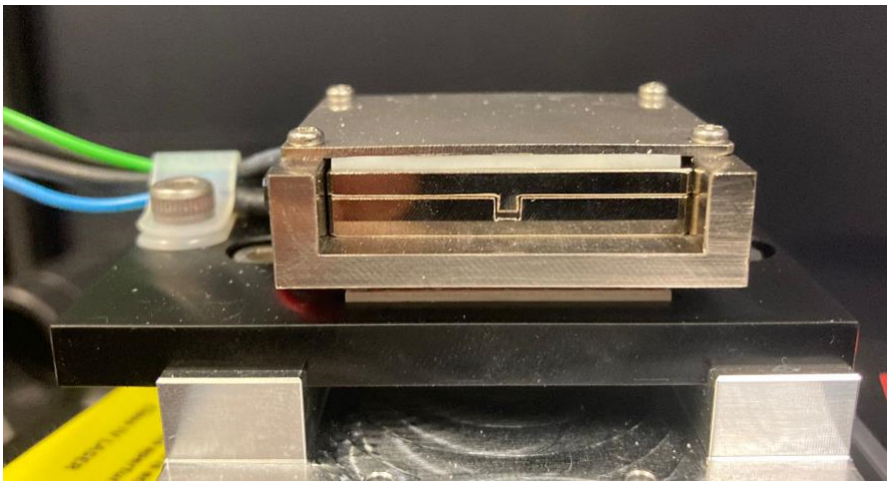

Figure 3.7: Housing of the nonlinear crystal supplied by oxide, including the Peltier element.

and can be seen in Figure 3.7. We will use the TEC1091 Peltier control module from *Meerstetter Engineering*[6] with this Peltier element. With these components, we achieve a temperature stability of 0.002 °C. Note that the temperature stability also depends on the stability of the ambient air temperature and how sheltered the crystal is from air currents.

a schematic of the initial test setup we used to verify that all calculations are correct and that we are able to achieve the desired output power can be seen in Figure 3.8. As a note here, it was more or less expected to deviate from the calculated values for QPMT, as this was also the case in Refs. [30, 27, 31]. The crystal housing is mounted on a translation stage (y-direction, see setup schematic) and a rotation stage, in order to adjust the angle and the position at which the beam enters the crystal. These stages are then mounted on an optical rail from Owis[7], in order to adjust the beam waist position within the crystal. A cage system is used for translating the lens L1 in beam direction, in order to adjust the beam waist. The lens L2 is mounted on a xy-translation stage, because it was mentioned in Ref. [30] that being able to adjust the lens position in the xy-plane is very valuable to obtain the optimal phase matching condition.

Measurements with test setup

With the test setup we were able to obtain 11.55 W of second harmonic at a pump power of 32 W. This equates to a SHG efficiency of 36 %. The full measurement can be seen in Figure 3.9. In this measurement, the beam waist was 28.2 µm. This was measured by first measuring the spot size at different positions with a beam profiler mounted on the optical rail, and then extracting the beam waist from a fit. At low input power, we achieved an efficiency gain of 2.56 %/W. Saturation effects due to pump depletion and thermal effects are visible. We also measured the temperature bandwidth and found $T_{\mathrm{FWHM}} = 1.03\,^{\circ}\mathrm{C}$. During the high-power measurement, the crystal broke at an input power of 35 W. We found that during the alignment process, where we went for the highest output power possible (alignment was performed at 250 mW input power), the beam entrance position shifted far towards the edge of the input face, without us noticing. This probably caused a very asymmetric temperature load, which lead to the breaking of the crystal. In a follow-up measurement, we made sure the beam enters the crystal as center as possible, and were able to go up to 35 W of input power without breaking the crystal and measured 12.91 W second harmonic power.

[6] https://meerstetter.ch

[7] https://owis.eu/, S25LL. We designed a connecting piece between optical rail and crystal mount. It was mill-cut by the D-PHYS workshop at ETH.

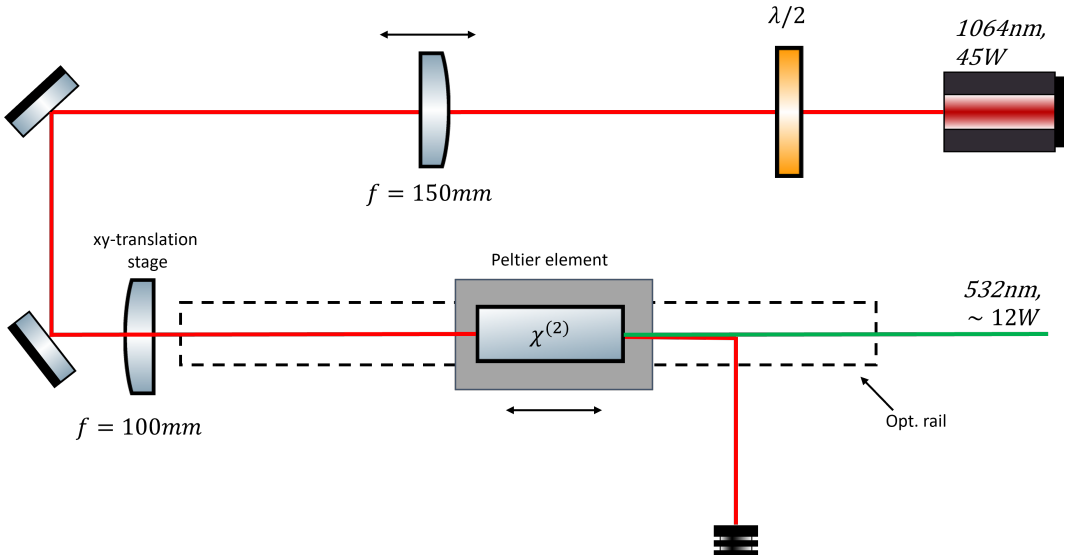

Figure 3.8: Schematic of the test setup. The $\lambda/2$ waveplate is used to polarize the pump field along the direction with highest nonlinear coefficient. The first lens is mounted on a cage system to tune the beam waist. The two mirrors are used to center the beam along the optical rail on which the crystal is mounted. We use a xy-translation stage for the second lens (z-position is fixed; z-direction is always along the beam). The crystal housing with Peltier element is mounted on a y-translation stage and a rotation stage (rotation in the yz-plane). The dichroic mirror then separates the second harmonic from the remaining pump field.

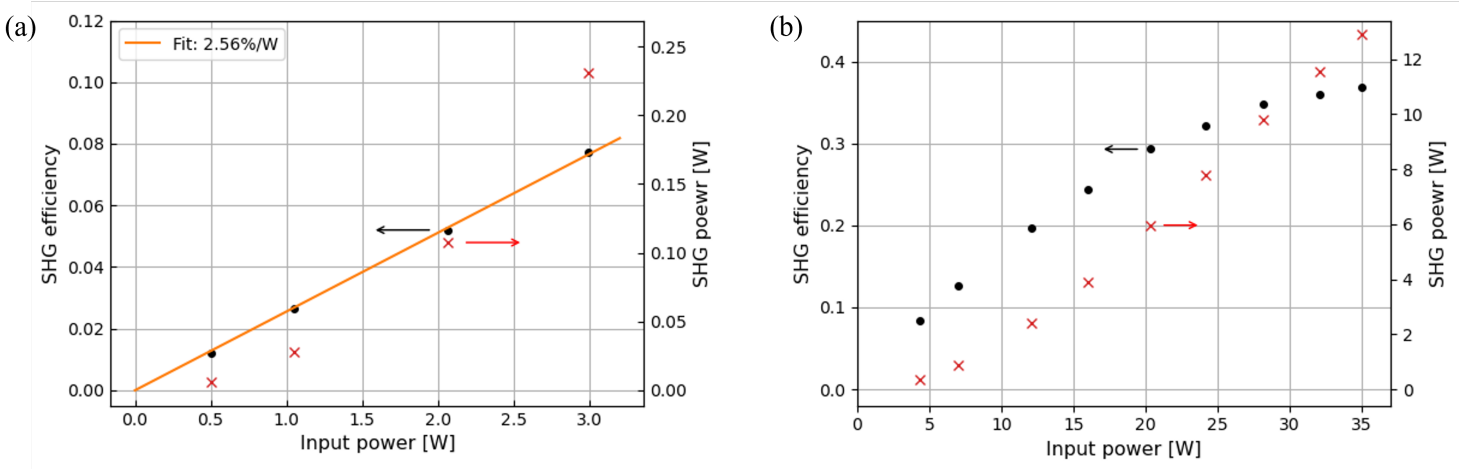

Figure 3.9: Measurements performed on the test setup at beam waist 29 µm. (a) Conversion efficiency and SH power at low power as function of input power. Black dots indicate measured efficiency, red crosses indicate measured SH power. Linear fit of efficiency gives an efficiency gain of 2.56 W/%. (b) SHG efficiency and power at high power as function of input power. Solid orange linear fit of efficiency at low input power. Dotted fit of the SHG power. Blue is a quadratic fit for low power, green is a linear fit for high power. We see that the efficiency quickly starts to saturate at input powers above 20 W. We achieve a maximum SH power of 12.91 W at 35 W input power.

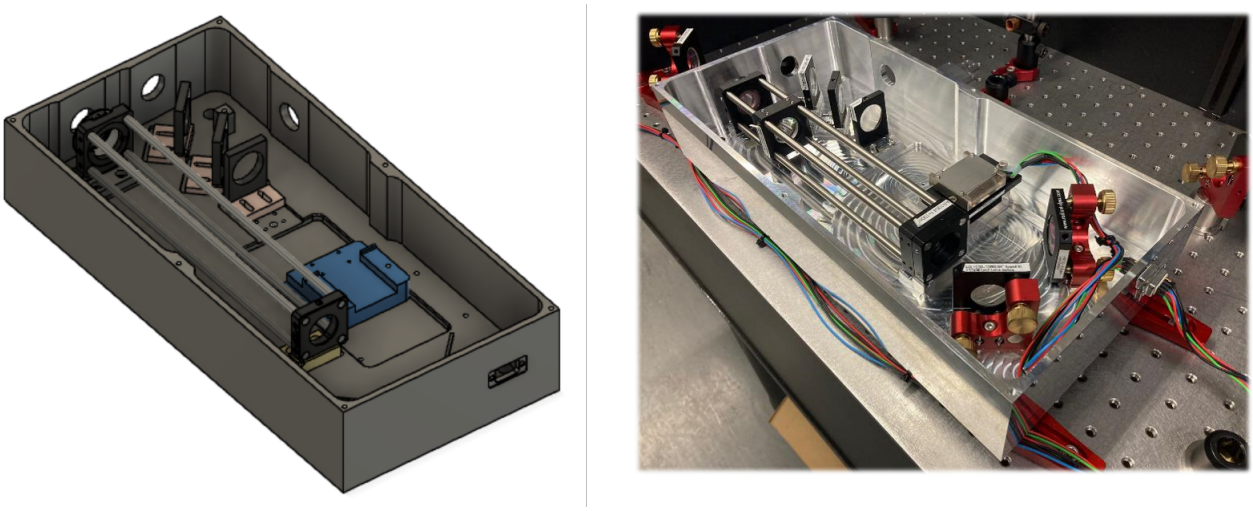

Figure 3.10: Design and final 'product' of the monolithic setup (top plate is not shown here). The crystal is mounted on the blue slider that can be used to position the waist in the center of the crystal. In this setup, only the two mirrors are used to align the beam in the crystal; there is no translation- or rotation stage. Both lenses are mounted in a cage system (Thorlabs, length 250 mm). We have placed both lenses before the mirrors, so the beam is always in the center of the lenses, which increases beam quality.

3.4 Monolithic design

After ensuring the SHG setup allows the correct alignment of the crystal and we are able to reach the desired output power with sufficient stability, we designed a monolithic and closed setup with the least amount of degrees of freedom as possible. This ensures an easier alignment process and, more importantly, shields the components from air currents and dust. The former improves temperature and hence power stability, but especially the latter is important for longtime operation of the setup, since we are dealing with highly focused and high power laser beams. The setup was designed in Fusion 360[8] and manufactured by the D-PHYS workshop at ETH. It is mill-cut from a single block of aluminium. The design and the final product can be seen in Figure 3.10. The input and output ports for the laser beams will be sealed with 1064 nm and 532 nm anti-reflection coated windows. The major change with respect to the test setup is the removal of the y-translation- and rotation stage for the crystal, and putting both lenses on the cage system in front of both adjustable mirrors. Since the alignment in this new design will be exclusively performed with just the two mirrors in front of the crystal, having no lens after the mirrors will simplify this process. The crystal mount is placed on a slider that can be used to adjust the focus position in the crystal. There is also the possibility to mount the beam profiler camera on the slider in order to be able to measure the beam waist, as described above. The first mount after the crystal houses a lens that is used to collimate the beam again after it was focused to $\sim$30 µm. The last two mounts are used for dichroic mirrors to separate the fundamental from the second harmonic. Both beams are then led out through windows on different sides of the cube. All windows are mounted at an angle of 3° to avoid direct back reflection.

Alignment procedure

The monolith was designed such that the alignment is as easy as possible. The most important tool for that is a beam profiler camera, which can be screwed onto the crystal mount. The first step is to couple the pump laser beam as center as possible into the cage system. This is best done without the lenses in the cage system. For this one can use two iris mounted onto the cage

[8] https://audodesk.com

posts (see Figure 3.10 for designations) and the beam profiler camera. After aligning the incoming beam by eye, one uses the two mirrors in the setup to direct the beam onto the camera. Then by iteratively closing the iris, one can see where the beam is cut off, and using two external coupling mirrors to counteract this cutting off. When both iris can be closed almost completely without unevenly cutting off the beam, the input beam is aligned with the axis of the monolith.

The next step is to establish the correct beam waist. The beam profiler mounted onto the crystal mount can be used to measure the beam diameter at different points along the slider. With these measurements one can fit the beam waist and waist position.

Then the pump beam has to be aligned with the crystal. This is very easy due to the design of the setup. Again, the camera should be used to ensure the beam is parallel to the crystal axis. When the beam traverses the crystal in the center and is parallel to the setup axis, one already should have established a good conversion efficiency. After that, only fine-tuning with the two mirrors and lenses is necessary.

3.5 Measurements

We performed several characterization measurements on the monolithic setup. First and foremost we want to make sure we can reach the desired output power. Therefore we measured the SHG efficiency as a function of input power up to 35 W for different beam waists. The results can be seen in Figure 3.11. Figure (a) shows the efficiency measurement at low power to check proper alignment for the optimal waist of 29 µm. The manufacturer states that an efficiency gain of $\sim 2\,\%/\mathrm{W}$ is expected. We use a linear fit on our data and observe a gain of[9] $2.07\,\%/\mathrm{W}$ and also a very good agreement to the undepleted pump approximation for low power input (linear increase in efficiency). Figure (b) shows the efficiency for different beam waists. As expected by our calculations, the highest efficiency at low power is obtained with a waist of 29 µm. But thermal effects already set in at an input power of 20 W. The efficiency gain is almost completely saturated at 35 W input power. Increasing the waist to 36 µm decreases the efficiency gain at low power as expected, but due to the mitigation of thermal effects, saturation effects set in only at much higher input powers. This results in a higher efficiency at an input power of 28 W and above. With this configuration we reach an efficiency of 40.6 %, which equates to an absolute output power of 14.10 W at an input power of 34.75 W. A waist of 46 µm shows even more saturation than the 36 µm waist, which is surprising.

This measurement shows that we can quite comfortably reach the required output power of 12 W. A repeat of this measurement with more beam waists and also measuring the efficiency at 35 W at the best beam waist as a function of waist position in the crystal will probably increase the maximum efficiency even further. This would allow us to use less input power to reach the 12 W.

Next we investigated the beam profile of the second harmonic at different distances from the output port of the monolith. A collage of the beam shape between 50 cm and 300 cm for 1.3 mW SH power can be seen in Figure 3.12. We see that the profile is still Gaussian in shape. Note that the fringes in the intensity are an artefact of the camera filters. At 200 cm, the beam starts to get slightly elliptical, but the ellipticity never got beyond 1.27. For us of course the beam profile at high power is more important. In order to do this measurement without destroying the beam profiler, we used an anti-reflection coated glass plate, placed it at an angle in the beam path and captured the reflection. Figure 3.13 shows the resulting beam profile for 5.2 W of SH power. There is no visible change compared to the lower output power. It was expected from theory that the second harmonic beam has a Gaussian envelope, but does deviate from a Gaussian beam (in that it has a smaller waist while having less divergence than the pump beam) [15]. It is expected to do so by

[9] Note that we reported an efficiency gain of $2.56\,\%/\mathrm{W}$ in the test setup. This discrepancy is due to the measurements being performed with different power heads.

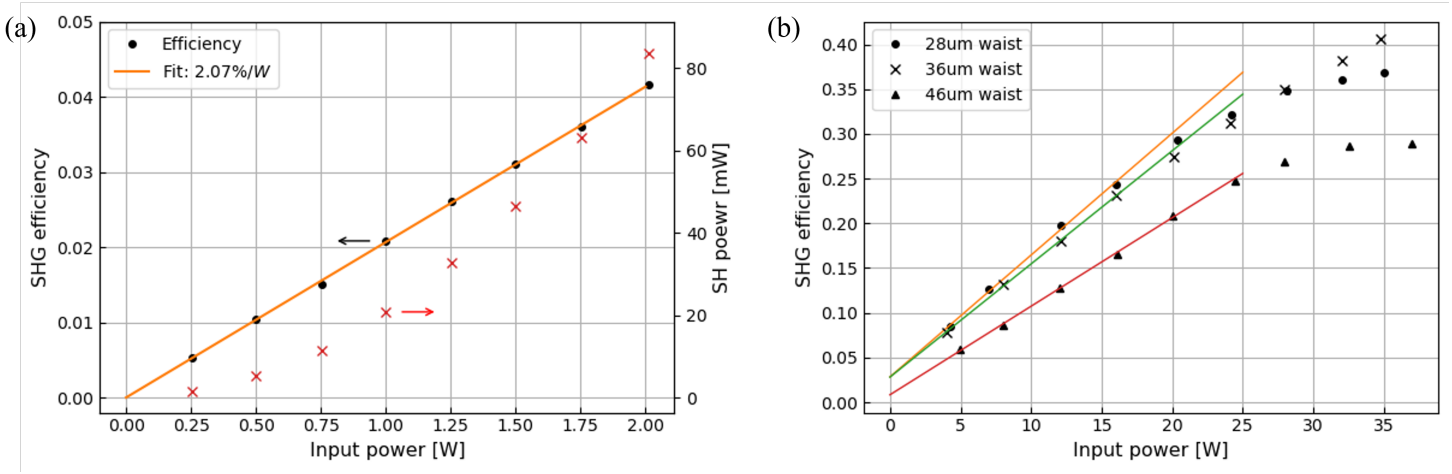

Figure 3.11: Efficiency measurement performed on the monolithic setup. (a) Low power efficiency measurement. Black dots indicate measured efficiency, red crosses indicate measured SH power. We achieve an efficiency gain of 2.07 W/%. (b) High power efficiency measurement for three different beam waists with linear fits. Orange fit belongs to 29 µm beam waist, green to 36 µm and red to 46 µm waist. The optimal beam waist 29 µm gives the highest efficiency gain at low power, but suffers from thermal effects at powers above 20 W, which saturate the efficiency gain. A beam waist of 36 µm has lower efficiency gain at high power, but due to the increased beam waist, the temperature gradient in the crystal is reduced, and hence the efficiency gain does not saturate as fast as for the 29 µm beam waist. With this we achieve the highest measured SH power of 14.1 W at an input power of 34.75 W. Increasing the beam waist further to 46 µm did not show benefits in the low nor the high power regime.

having a smaller waist while being less divergent.

Finally, we measured the output power over a longer period of time at high input power. Here we again measure a reflected beam from an AR-coated glass plate. This has two reasons: first, we avoid potentially damaging the power head, and second, we can use a smaller power head that is more sensitive to fast disturbances. Initially, we wanted to start with a two hour long measurement. But after a small 10 minute test run, we discovered the output power dropped by 10 % in these 10 minutes. The measurement can be seen in Figure 3.14 (a). We use a Python script in combination with a PicoScope[10] in order to periodically measure the output voltage of the power meter. Therefore, the y-axis in the plots are normalized to the measured voltage at $t = 0$, since the absolute value of this voltage is not meaningful (in general, the measured power is not important for this measurement, but more the relative fluctuation). The Python script also records the measured temperature, which shows there is no fluctuation in temperature that could cause this behaviour. By increasing the temperature setpoint, we were able to restore the original efficiency. After another 10 minutes, the same decrease in efficiency was observed. This went on for three more runs, until a 10 minute run measured stable efficiency. This can be seen in Figure 3.14 (c). Here we achieve very good stability over 10 minutes, with the largest fluctuation being 0.1 % of the power measured at $t = 0$. It is in principle not surprising that, at higher input power, the QPMT changes slightly when starting with the pumping. As can be seen, we had to increase the temperature setpoint by almost 0.5 °C. But what we can not explain is, why the decrease in output power happens very quickly, after which it again plateaus.

After finding a temperature setpoint that stabilized the output power over 10 minutes, we measured the stability for two hours. The result can be seen in Figure 3.15. Here we also observe these quick

[10] https://picot

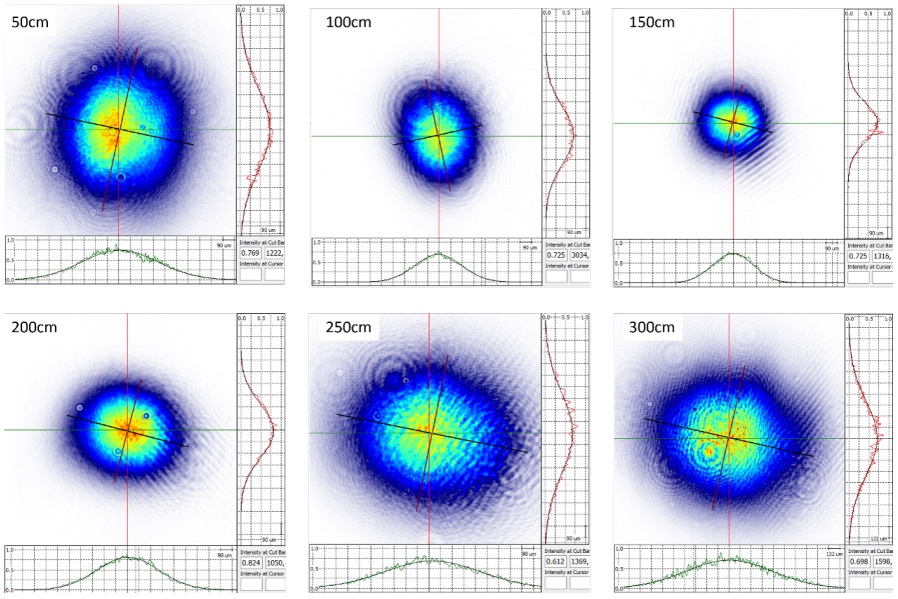

Figure 3.12: Beam profile for 1.3 mW output power at different distances from the output window of the monolithic setup. Note that the images are not to scale (see the raster on the bottom and right of each image for scale). We observe very nice Gaussian beam shapes at all distances. At distances above 150 cm the beams become slightly elliptical.

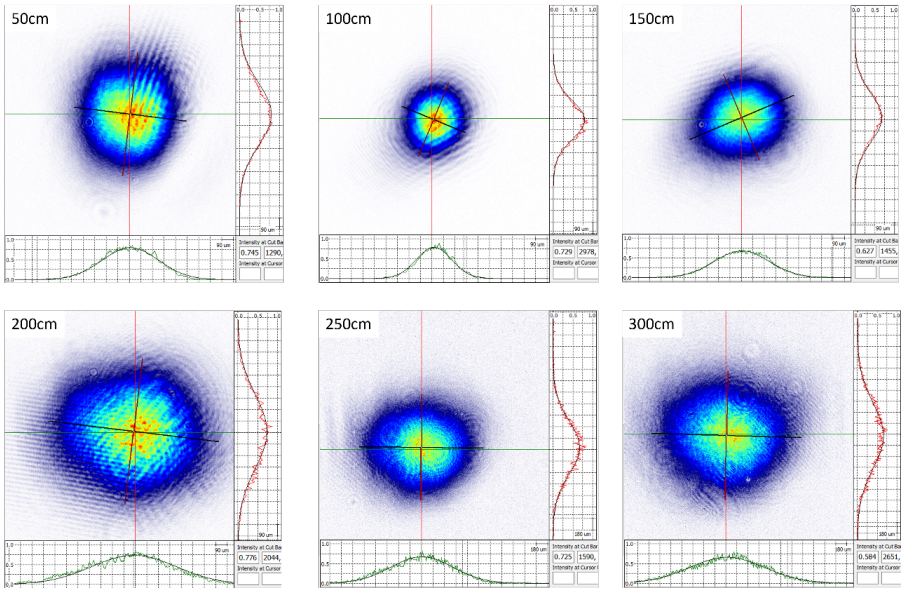

Figure 3.13: Beam profile for 5.2 W output power at different distances from the output window of the monolithic setup. Note that the images are not to scale (see the raster on the bottom and right of each image for scale). There is no visible change to the beam shape compared to the low power measurements.

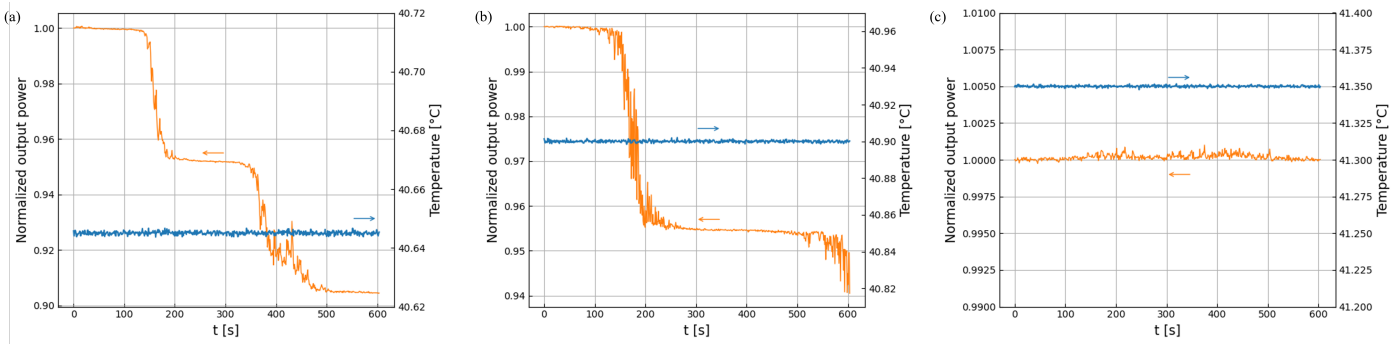

Figure 3.14: Successive 10 min measurements of output power (1 Hz sample rate). The orange line shows measured power and blue line shows measured temperature. (a) shows the first measurement, (b) the following and (c) shows the fifth 10 min measurement. After a period of very stable output power, it decreases very quickly by $\sim 4\,\%$ in a time span of $\sim 30\,\mathrm{s} - 100\,\mathrm{s}$. After every measurement, we are able to restore the initial efficiency by increasing the temperature setpoint. Repeating this four times, the output power is stable over the full 10 min.

descends of output power, followed by relatively stable plateaus. But in comparison to the previous runs, the plateaus are much longer. Figure 3.15 (b) shows a zoom-in into the first plateau. We see that we have excellent stability, with fluctiations less than $0.2\,\%$, over 20 min. Due to time constraints we were not able to repeat these measurements or increase the measured time period. We suspect that the jumps between plateaus are caused by mode jumps of the seed laser, but further measurements have to be performed in order to confirm this suspicion.

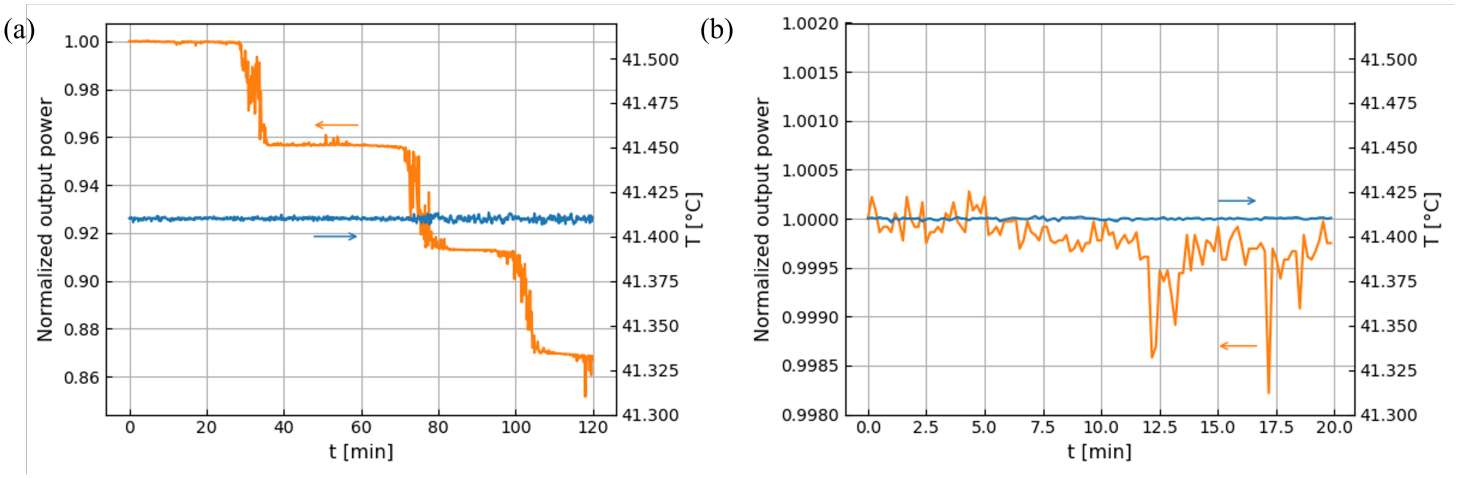

Figure 3.15: (a) Output power observed over 2 h after the five 10 min measurements. We again see the same plateaus as in the previous measurement, just with longer stable periods. (b) Zoom-in into the first 20 min of the measurement. Here we see excellent stability, with fluctuations less than 0.2 %. Also after this measurement we were able to recover the initial efficiency by increasing the temperature to 41.8 °C.

Chapter 4

Conclusion

The goal of this thesis was to further develop the active control scheme necessary for the superlattice accordion developed in Ref. [13]. In conjunction with that, the development, testing and 'product' design of a second harmonic generation setup as the laser source for the 532 nm lattice beams was also part of this thesis. For this purpose, a power of 12 W is required.

In the first part we developed the theory necessary for the phase measurement of the lattice beams for two-dimensional lattices. We also showed that we can treat the two superimposed lattices separately. We found that the naive approach of extracting the phases from the FFT of the full lattice is not robust against intensity fluctuations of the laser beams. In order to solve this problem, we introduced the shutter method. There, we periodically block two of the four lattice beams to calculate the relative phase of the unblocked beams analog to the one-dimensional case. This additional relative phase in combination with the relative phases extracted from the full lattice allows us to calculate the phase of all four lattice beams. We then wrote a simulation of the phase extraction to verify its correctness, and also to gauge the necessary camera specifications. We found a phase measurement error smaller than 0.01 rad for all phases.

Then we presented our research for the optimal frequency source for driving the AODs, which will be used to control the lattice constant and position. We found that the requirement of having a flexible digital input that can deal with user defined data is only really fulfilled by the USRP N310 from Ettus Research. It is a Software Defined Radio (SDR) based device with an on-board FPGA that can be fully customized. This allows us to use the hardware part of the device with our own custom signal processing running on the FPGA. We will synthesize all eight driving tones on the FPGA and send the amplitude and frequency information from a PC to the device via Ethernet. The FPGA has full access to the digital input, over which we will send the phase control signal using a serial protocol. Due to time constraints, we did not build or implement a setup for the feedback scheme.

In the third chapter we presented the design for the second harmonic generation setup we developed. We started the chapter with an overview over the theory of second harmonic generation, and showed how we calculated the experimental parameters one has to establish in order to achieve high conversion efficiency. The nonlinear crystal that was used here is a 5 % MgO doped sPPLT from Oxide with a poling period of 7.98 µm. With the Sellmeier equation for the refractive index (parameters taken from Ref. [25]), we calculated a phase matching temperature of 51 °C and an optimal beam waist of 29 µm. Experimentally, we were able confirm the optimal beam waist at low input powers, but found a phase matching temperature of 41 °C. This discrepancy in phase matching temperature between theory and experiment is often observed (see Refs. [30, 27, 31])

and can be explained by fabrication imperfections. At higher input powers, we observed saturation of efficiency gain at the optimal beam waist of 29 µm. Loosening the focus to 36 µm, we achieved a maximal second harmonic power of 14.1 W at an input power of 34.75 W. This equates to a conversion efficiency of 40.5 %. This was expected, since thermal effects are decreased by choosing a wider beam waist. We also designed a monolithic setup that is mill-cut from a single block of aluminium. The input and output ports are sealed with anti-reflection coated windows. This will create a dust free environment, which will increase the expected life time of all optical elements significantly. In addition to that, this also helps with temperature stability. With this setup, we achieve temperature stabilization with an accuracy of 0.002 °C. After measuring the stability over 2 h, we found periods of very good stability with fluctuations smaller than 0.2 %. But after $\sim$ 20 min, the output power decreased by 4 % within a short period of time, followed again by a period of stable output power. We suspect mode jumps of the seed laser of the pump laser to be responsible for these sharp transitions, but were not yet able to confirm it and more investigations are necessary.

The next steps towards the realization of the superlattice accordion are to build a setup for the active stabilization and implement the driving tone synthesis for the AODs on the FPGA of the USRP N310. In the simulation of the phase extraction we tried to make the situation as close to reality as possible by adding noise and quantization error. But nevertheless, only the implementation on real hardware and building an optical test setup can tell whether this approach is feasible. For the second harmonic generation, the reason behind the rapid decline in output power has to be investigated. In addition to that, more efficiency measurements with beam waists between 36 µm and 29 µm could reveal a more optimal beam waist for high power than 36 µm. Also, due to time constraints we have not investigated the impact of the waist position in the crystal on efficiency at high input power. In is expected that the efficiency at high power increases when the waist position is shifted slightly towards the input face of the crystal, due to reduced green-induced infrared absorption (GRIIRA) [27]. Decreasing the necessary input power for achieving the 12 W output power would further improve beam quality.

Acknowledgements

My last six months at ETH has been one of the most exciting and interesting periods of my studies. Many thanks are in order, and I want to start with my supervisors Dr. Konrad Viebahn and Marius Gächter, for composing such an interesting and multifaceted project, for many invigorating discussions and of course for having seemingly endless patience, when something does not go to plan. My gratitude also goes to the rest of the Quantum Optics group for creating such a relaxed and inspiring work environment. A special thank you to Philipp Fabritius and Myles Huang from the Lithium Team for sharing their vast knowledge and experience when it comes to troubleshooting second harmonic generation setups. Also a massive thank you to Prof. Tilman Esslinger, not only for giving me the opportunity to conduct my master thesis at his group, but also for always having an open door to listen to everyones needs and questions. Last but not least I want to thank my family and friends, for supporting me through all of my studies, for suffering with me through hard exam sessions and also for celebrating – no matter the result.

Bibliography

[1] Richard P Feynman. Simulating physics with computers. *International Journal of Theoretical Physics*, 21(6/7), 1981.

[2] Morten Kjaergaard, Mollie E Schwartz, Jochen Braumüller, Philip Krantz, Joel I-J Wang, Simon Gustavsson, and William D Oliver. Superconducting qubits: Current state of play. *Annual Review of Condensed Matter Physics*, 11:369–395, 2020.

[3] Christoph Kloeffel and Daniel Loss. Prospects for spin-based quantum computing in quantum dots. *Annu. Rev. Condens. Matter Phys.*, 4(1):51–81, 2013.

[4] Simon C Benjamin and Jason M Smith. Driving a hard bargain with diamond qubits. *Physics*, 4:78, 2011.

[5] John Hubbard. Electron correlations in narrow energy bands. *Proc. R. Soc. London*, 1963.

[6] AS Walter, Z Zhu, M Gächter, J Minguzzi, S Roschinski, K Sandholzer, K Viebahn, and T Esslinger. Quantisation and its breakdown in a hubbard-thouless pump. *arXiv preprint arXiv:2204.06561*, 2022.

[7] Zijie Zhu, Marius Gächter, Anne-Sophie Walter, Konrad Viebahn, and Tilman Esslinger. Reversal of quantised hall drifts at non-interacting and interacting topological boundaries, 2023.

[8] Joaquín Minguzzi, Zijie Zhu, Kilian Sandholzer, Anne-Sophie Walter, Konrad Viebahn, and Tilman Esslinger. Topological pumping in a floquet-bloch band. *Phys. Rev. Lett.*, 129:053201, Jul 2022.

[9] J. Bonca, P. Prelovsek, A. Ramsak, and S. Sarkar. *Open Problems in Strongly Correlated Electron Systems*. Springer, 2001.

[10] Florian Schäfer, Takeshi Fukuhara, Seiji Sugawa, Yosuke Takasu, and Yoshiro Takahashi. Tools for quantum simulation with ultracold atoms in optical lattices. *Nature Reviews Physics*, 2(8):411–425, 2020.

[11] Neil W Ashcroft and N David Mermin. *Solid state physics*. Cengage Learning, 2022.

[12] Assa Auerbach. *Interacting electrons and quantum magnetism*. Springer Science & Business Media, 1998.

[13] Simon Wili, Tilman Esslinger, and Konrad Viebahn. An accordion superlattice for controlling atom separation in optical potentials. *New J. Phys., 25 033037*, 2023.

[14] S. Wili. A versatile accordion lattice setup for tweezers experiments. *ETH Zurich*, 2021.

[15] Robert Boyd. *Nonlinear Optics, 3rd Edition.* Academic Press, 2008.

[16] C.E. Shannon. Communication in the presence of noise. *Proceedings of the IRE*, 37(1):10–21, 1949.

[17] Bahaa E A Saleh and Malvin Carl Teich. *Fundamentals of photonics; 2nd ed.* Wiley series in pure and applied optics. Wiley, New York, NY, 2007.

[18] A. B. Cesar. MISSING CITATION! *Nature*, 1970.

[19] QBlox. https://www.qblox.com/ (accessed: 11.04.2023).

[20] Noah Berner. Printed circuit board design for direct digital synthesis. *ETH Zurich*, 2020.

[21] Fuqin Xiong. *Digital Modulation Techniques.* Artech House Telecommunications Library, 2006.

[22] Ettus Research. Products (accessed: 11.04.2023), https://www.ettus.com/products/.

[23] Ettus Research. Basictx daughterboard (accessed: 11.04.2023), https://www.ettus.com/all-products/basictx/.

[24] J. A. Armstrong, N. Bloembergen, J. Ducuing, and P. S. Pershan. Interactions between light waves in a nonlinear dielectric. *Phys. Rev.*, 127:1918–1939, Sep 1962.

[25] Ichiro Shoji, Yuki Iwamoto, Yuki Kagami, and Yasunori Furukawa. Temperature-dependent refractive indices of undoped and mgo-doped stoichiometric litao3 and their sellmeier equations. In *Optica Advanced Photonics Congress 2022*, page NoTh2E.3. Optica Publishing Group, 2022.

[26] G. Boyd and D.A. Kleinman. Parametric interaction of focused gaussian light beams. *Journal of Applied Physics 39, 3597*, 1968.

[27] S. Chaitanya Kumar, G. K. Samanta, and M. Ebrahim-Zadeh. High-power, single-frequency, continuous-wave second-harmonic-generation of ytterbium fiber laser in ppktp and mgo:spplt. *Opt. Express*, 17(16):13711–13726, Aug 2009.

[28] Ichiro Shoji, Takashi Kondo, Ayako Kitamoto, Masayuki Shirane, and Ryoichi Ito. Absolute scale of second-order nonlinear-optical coefficients. *J. Opt. Soc. Am. B*, 14(9):2268–2294, Sep 1997.

[29] M Stappel, R Steinborn, D Kolbe, and J Walz. A high power, continuous-wave, single-frequency fiber amplifier at 1091Å nm and frequency doubling to 545.5Å nm. *Laser Physics*, 23(7):075103, may 2013.

[30] Franco Rabec. A 671nm laser source, for a 6li cold atom experiment. *ETH Zurich*, 2020.

[31] Mukesh Kumar Shukla, Samir Kumar, and Ritwick Das. High-power, single-frequency, single-pass second-harmonic-generation by optimally focused yb-fiber laser. In *Advanced Solid State Lasers*, page ATh2A.22. Optica Publishing Group, 2014.